Process design of solid-liquid mixing in agitated vessels based on transport phenomena

越智，友亮

(Degree)
博士（工学）

(Date of Degree)
2022-03-25

(Date of Publication)
2023-03-01

(Resource Type)
doctoral thesis

(Report Number)
甲第8361号

(URL)
https://hdl.handle.net/20.500.14094/D1008361

Doctoral Dissertation

博士論文

Process design of solid-liquid mixing in
agitated vessels based on transport phenomena

移動現象論に基づいた固液撹拌槽プロセス
の設計に関する研究

Graduate School of Engineering, Kobe University

神戸大学大学院工学研究科

Yusuke Ochi

越智友亮

January, 2022

2022 年 1 月

Contents

ii

Chapter 1

General Introduction

1.1 Agitated Vessels

A chemical plant consists of many kinds of organically linked basic operations, so-called unit operations. Even in the recent chemical industries, where digital technologies have streamlined chemical plants, the performance of each unit operation dominates the productivity of the whole of a chemical plant. Mixing is one of the most common unit operations in various chemical processes with chemical reactions, extraction, crystallization, dispersion, or drying. The specific aims of the mixing process are to homogenize fluid temperature and material concentration and control the dispersion state of the dispersed phase. In addition, mixing devices deal with several operations simultaneously, such as chemical reactions and separation. Accordingly, enhancement of reaction and mass/heat transfer is also an essential objective of the mixing operation.

The conventional agitated vessel, also called mixing tank, is the most
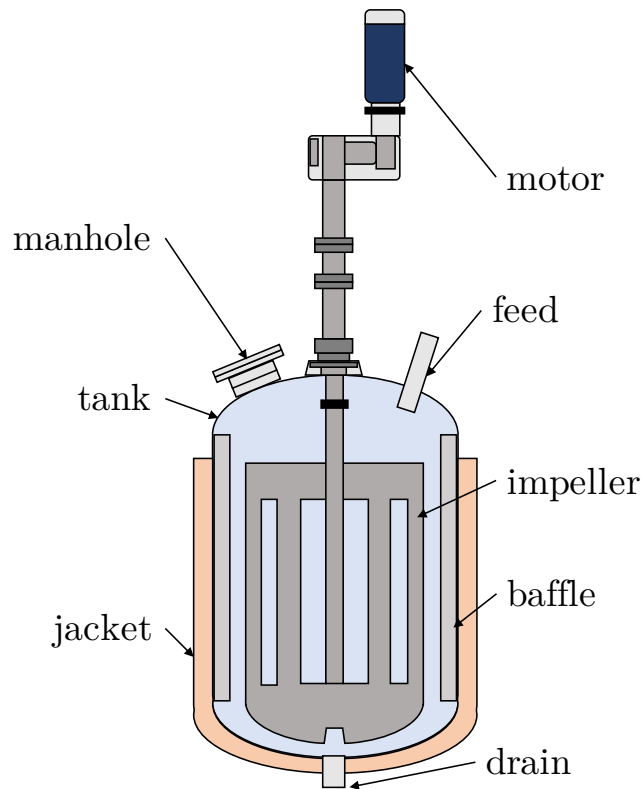
Figure 1.1: Typical configuration of a mixing tank reactor.

common mechanical mixing device containing a rotating impeller, baffles, a jacket or a coil for thermal control, and other measurement instruments as shown in Figure 1.1. The agitated vessel often plays a principal role in the process as a reactor for polymerization in the polymer industry[1] or fermenters in bio-industry,[2] due to the large throughput and high heat and mass transfer performance. In addition, agitated vessels are used supplementally in pre-treatment and post-treatment processes. Consequently, the mixing tank reactor often deals with multiphase flows with different physical characteristics, such as solid-liquid, liquid-liquid, gas-liquid and even gas-soild-liquid systems. Different properties of the agitated system lead to a wide variety

of requirements for processes. Hence, the optimal design of a mixing tank reactor is essential to accomplish an appropriate hydrodynamic state for the successful performance of the process. Additionally, the understanding of physical phenomena is necessary to realize the successful performance of the process.

1.1.1 Transport phenomena in an agitated vessel

The operation of the agitated vessel process looks simple, such as filling up the tank with the working fluid and rotating the impeller, but it is actually not. The complicated physical phenomena can be found in the agitated vessel and lead to difficulty designing agitated vessel processes. Therefore, it is essential to understand momentum, mass, and heat transfer and estimate consequently appearing characteristic properties, such as power consumption, mixing time, shear force, and heat and mass transfer coefficients.

Power consumption

The rotating impeller provides momentum and kinetic energy to the working fluid, and the fluid transports them to the vessel wall. In the laminar flow at low Reynolds numbers, the kinetic energy supplied to the fluid is directly converted to thermal energy. On the other hand, the kinetic energy is converted to turbulent energy before being converted to thermal energy in the turbulent flow. This thermal energy, in other words, dissipation energy, is equivalent to the power consumption of the rotating impeller, which is an essential variable to select an appropriate motor and estimate the different

kinds of effects of agitation on the process.

Nagata et al.[3] provided the most commonly-used empirical equation of the power number $N_\mathrm{p}(= P/\rho N^3 d^5)$ for paddle impellers having two blades in a non-baffled tank as follows.

$$N_\mathrm{p} = \frac{A}{Re_\mathrm{d}} + B \left(\frac{10^3 + 1.2 Re_\mathrm{d}^{0.66}}{10^3 + 3.2 Re_\mathrm{d}^{0.66}} \right)^p \left(\frac{H}{D} \right)^{0.35 + b/D} \tag{1.1}$$

where

$$A = 14 + \left(\frac{b}{D} \right) \left\{ 670 \left(\frac{d}{D} - 0.6 \right)^2 + 185 \right\} \tag{1.2}$$

$$B = 10^{\{1.3 - 4(b/D - 0.5)^2 - 1.14(d/D)\}} \tag{1.3}$$

$$p = 1.1 + 4 \left(\frac{b}{D} \right) - 2.5 \left(\frac{d}{D} - 0.5 \right)^2 - 7 \left(\frac{b}{D} \right)^4 \tag{1.4}$$

Substituting the following critical Reynolds number into Equation (1.1) yields the power number at the fully baffled condition.

$$Re_\mathrm{c} = \frac{25(d/D - 0.4)^2}{b/D} + \frac{b/D}{0.11 b/D - 0.0048} \tag{1.5}$$

Hiraoka and Ito[4] correlated the power consumption to the friction factor at the wall of the vessel f and the modified Reynolds number Re_G. Based on the model by Hiraoka and Ito,[4] Kamei et al.[5] proposed the following correlation equation, Equation (1.6), which gives a more accurate result for the non-baffled tank even in the case of $b'(= n_\mathrm{p} b/2) > H$.

$$N_\mathrm{p0} = \frac{1.2 \pi^4 \beta^2}{8 d^3 / (D^2 H)} f \tag{1.6}$$

4

$$f = \frac{C_{\mathrm{L}}}{Re_{\mathrm{G}}} + C_{\mathrm{t}} \left\{ \left(\frac{C_{\mathrm{tr}}}{Re_{\mathrm{G}}} + Re_{\mathrm{G}} \right)^{-1} + \left(\frac{f_\infty}{C_{\mathrm{t}}} \right)^{1/m} \right\}^m \tag{1.7}$$

$$Re_{\mathrm{G}} = \frac{\pi \eta \ln(D/d)}{4d/(\beta D)} Re_{\mathrm{d}} \tag{1.8}$$

$$Re_{\mathrm{d}} = \frac{\rho N d^2}{\mu} \tag{1.9}$$

$$C_{\mathrm{L}} = 0.215 \eta n_{\mathrm{p}} \frac{d}{H} \left\{ 1 - \left(\frac{d}{D} \right)^2 \right\} + 1.83 \frac{b \sin \theta}{H} \left(\frac{n_{\mathrm{p}}}{2 \sin \theta} \right)^{1/3} \tag{1.10}$$

$$C_{\mathrm{t}} = \left\{ (1.96 X^{1.19})^{-7.8} + 0.25^{-7.8} \right\}^{-1/7.8} \tag{1.11}$$

$$C_{\mathrm{tr}} = 23.8 \left(\frac{d}{D} \right)^{-3.24} \left(\frac{b \sin \theta}{D} \right)^{-1.18} X^{0.74} \tag{1.12}$$

$$m = \left\{ (0.71 X^{0.373})^{-7.8} + 0.333^{-7.8} \right\}^{-1/7.8} \tag{1.13}$$

$$f_\infty = 0.0151 (d/D) C_{\mathrm{t}}^{0.308} \tag{1.14}$$

$$X = \frac{\gamma n_{\mathrm{p}}^{0.7} b \sin^{1.6} \theta}{H} \tag{1.15}$$

$$\beta = \frac{2 \ln (D/d)}{D/d - d/D} \tag{1.16}$$

$$\gamma = \left\{ \frac{\eta \ln(D/d)}{(\beta D/d)^5} \right\}^{1/3} \tag{1.17}$$

$$\eta = 0.711 \frac{0.157 + \{ n_{\mathrm{p}} \ln(D/d) \}^{0.611}}{n_{\mathrm{p}}^{0.52} \{ 1 - (d/D)^2 \}} \tag{1.18}$$

For baffled conditions, Kamei et al.[6] provided the following estimation.

$$N_{\mathrm{p}} = \{ (1 + x^{-3})^{-1/3} \} N_{\mathrm{p,max}} \tag{1.19}$$

$$x = 4.5 \left(\frac{B_{\mathrm{W}}}{D} \right) n_{\mathrm{B}} \frac{H/D}{N_{\mathrm{p,max}}^{0.2}} + \frac{N_{\mathrm{p0}}}{N_{\mathrm{p,max}}} \tag{1.20}$$

$$\left(\frac{B_{\mathrm{W}}}{D} \right) n_{\mathrm{B}}^{0.8} = 0.27 N_{\mathrm{p,max}} \tag{1.21}$$

Some successful modifications of the correlation by Kamei et al. can be found

for the pitched paddle,[7] propeller/pfaudler,[8] and large impellers.[9]

Mixing time

Mixing time, defined as the time required to achieve a complete homogenization, is a significant parameter to evaluate the mixing performance of a mixing process. Several experimental techniques have been developed to estimate the mixing time, such as colorimetry, electrical residence tomography, planer laser-induced fluorescence, thermography, conductometry, and pH measurement.[10] The non-dimensional mixing time Nt_{M} for the turbulent flow can be usually correlated to the power number N_{p}.[11,12] On the other hand, in the laminar flow, Nt_{M} decrease proportionally as the increase in $N_{\mathrm{p}}Re_{\mathrm{d}}$.[13,14]

Heat transfer

Several chemical reactions need high thermal controllability to enhance the reaction rate or remove heat for process safety. Helical coils are typically used to control the temperature in the tank for their high thermal efficiency. Heat transfer in the agitated tank with a helical coil has been experimentally and numerically studied for Newtonian and non-Newtonian fluids.[15–17] On the other hand, the heat transfer through the sidewall of the tank is often conducted in order to simplify the geometry of the tank and for the ease of cleaning. Heat transfer coefficients of the vessel wall have been, therefore, investigated by many researchers.[18–21] One of the most common estimations of heat transfer in the turbulent regime is the semiempirical non-dimensional

equation, Equation (1.22), in the form of the Nusselt number.[22]

$$Nu = KRe_{\mathrm{d}}^{2/3}Pr^{1/3}(\mu/\mu_{\mathrm{w}})^{0.14} \tag{1.22}$$

The coefficient K depends on the impeller configuration so that many values have been proposed for various impellers.[23–25]

1.1.2   Geometric design of an agitated vessel

Among the pieces of equipment in the agitated vessel, the impeller, baffle, and tank may control the hydrodynamics in the vessel. Therefore, literature has investigated the optimal design of the equipment.

Impeller

The impeller is the centerpiece of the mixing tank reactor since the impeller geometry and its operational condition have the most significant impacts on the process performance. Various types of impellers have been therefore designed to achieve the specific needs of the process. Impellers can be classified with the flow state according to the impeller Reynolds number Re_{d}.

At high Reynolds numbers, the hydrodynamic flow in the vessel becomes turbulent where the small impeller is often used. Small impellers are classified into two types, i.e., radial-flow and axial-flow types. The radial-flow type impellers, such as paddle, disk turbine, and pfaudler impellers, with vertically attached blades discharge fluid to the radial direction by its rotating motion. Then the fluid flow collides against the sidewall of the vessel and separates into upward and downward flows, which forms two circulations in the vessel

and leads to the superior mixing. The axial-flow type impellers, such as propeller, pitched paddle, and A310 impellers, discharge fluid to the axial direction and form a single circulation flow pattern. This flow pattern has an advantage in suspending solid particles being sunk in the vessel.

When the flow condition turns into the laminar regime as the decrease of Reynolds number, anchor, helical ribbon, and helical screw impellers are used instead of small impellers. These impellers can be found in many industrial processes, e.g., paint, polymers, and food. The standard anchor impeller has two vertical blades closely located to the vessel wall, which promotes heat transfer from the vessel wall. However, it is well known that the anchor impeller offers a weak secondary circulation flow in the vertical direction, so that recently some optimal asymmetric configurations of the anchor impeller were proposed to obtain sufficient mixing.[26] Helical ribbon and helical screw impellers have close-clearance with the vessel wall and provide a stronger vertical circulation than anchor impellers. An extensive literature has investigated the geometrical features of helical ribbon and helical screw impellers and their mixing performance.[27–29]

One strategy to deal with flows in a wide range of Reynolds numbers uses multi-impellers advocated by Western manufacturers. On the other hand, since the 1980s, a Japanese manufacturer, Sumitomo Heavy Industries Process Equipment Co., Ltd., has developed a large impeller, MAXBLEND®,[30] which has different mixing mechanisms from multi-impellers. Afterward, various types of large impellers have been launched, such as FULLZONE® by Kobelco Eco-Solutions Co.,Ltd., Super-Mix by SATAKE MultiMix Corporation, and Hi-F Mixer by Soken Tecnix Co., Ltd.

8
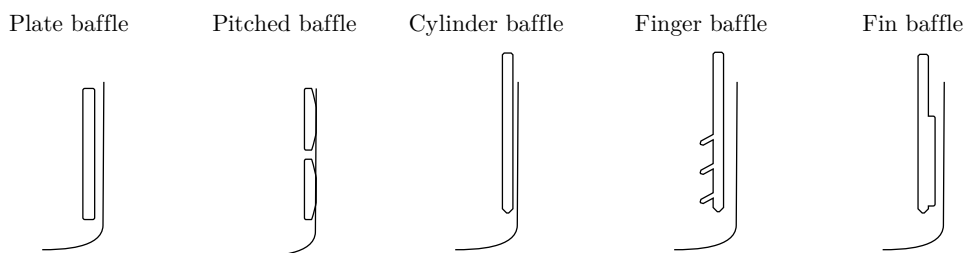
Figure 1.2: Typical configuration of baffles.

MAXBLEND® is the plate-shaped impeller which consists of the bottom paddle and the upper grid. The hydrodynamic characteristics of the MAXBLEND® impeller, which typically generates a vertical circulating flow pattern, have been investigated in laminar[31,32] and turbulent[33,34] regions and in both Newtonian and non-Newtonian fluids.[35,36] MAXBLEND® shows superior performance in many kinds of processes due to its high pumping capacity, uniform shear field, and good gas-liquid contact ability.[31,37,38] Moreover, MAXBLEND® impeller can be applied to a bio-reactor, and many experimental works revealed the high productivity of bio-material using the MAXBLEND® impeller.[39–41]

Baffle

Figure 1.2 illustrates different kinds of baffles.[42] Although the impeller selection is, of course, essential in a mixing tank reactor, the design of baffles is also important because baffles significantly affect the hydrodynamic condition in the vessel. Nevertheless, engineers' interest in baffles is often less than that in impellers. The standard baffle condition, four plate baffles one-tenth width of the diameter of the vessel, is widely adopted as a tacit understanding.

This baffle condition improves mixing by eliminating the vortex, often being formed in the agitated vessel agitated at a high rotational speed. Moreover, in processes with buoyant particles, not only the impeller type but also the baffle configuration plays an important role in dispersing particles. Khazam and Kresta[43] pointed out that surface baffles offered a significant reduction in the critical agitation speed for just drawdown of floating particles. Atibeni et al.[44] found that the triangular baffles performed better for the drawdown of floating particles than either standard baffles or narrow baffles. On the other hand, with settling particles, bottom baffles are widely used to disperse particles.[45] Regarding the baffle type, Major-Godlewska and Karcz[46] experimentally investigated the effect of the configuration of tubular baffles on the power consumption using five different small impellers. In the laminar flow region where the vortex is not formed, Kato et al.[47] and Wang et al.[48] reported that isolated mixing regions could be drastically eliminated with the installation of baffles at low Reynolds numbers using a visual decolorization technique. Inoue et al.[49] explained that the deformation of streakline occurring around baffles contributes to eliminating the isolated mixing regions and to enhancing mixing in the laminar flow in an agitated vessel. Furthermore, as to the power consumption, Kato et al.[50] investigated the effect of the baffle length on the power consumption with several impellers and modified the correlation equation between the Reynolds number and the power number.

As described above, recently, baffles have got attention and been investigated to control and improve processes in the agitated vessel. However, the effect of baffle configuration on the hydrodynamics and transport phenomena in the vessel has not been sufficiently understood. Especially, the clearance

10

between a baffle and the sidewall of the vessel has not been studied enough, although Furukawa et al.[51,52] investigated the effect of baffle clearance on mixing.

Vessel

The volumetric capacity of the tank and H/D are crucial factors for the design of the tank, where H is the liquid height, and D is the diameter of the tank, respectively.[42] As H/D increases, the heat transfer area per tank volume increases. However, the vertical circulation flow may become poor, which affects the mixing performance. Besides, the mixing shaft should be larger in diameter. In contrast, if H/D is small, the board thickness of the vessel must be large, which leads to an increase in the material cost. A mixing tank reactor is generally designed to satisfy $H/D = 1$–1.5. As a reactor, high pressure in the vessel limits its configuration. Thus, the effect of the geometric configuration of the vessel on flow characteristics has not been studied in detail. For particulate processes, some shapes of the bottom of the vessel were investigated to suspend solid particles.[53]

1.2 Solid-liquid process in an agitated vessel

Many industries deal with solid-liquid multiphase processes in agitated vessels, such as agglomeration of solid particles, mineral treatment, crystallization, preparation of the slurry, and synthesis of chemicals using solid catalysts. Consequently, different issues can be found in solid-liquid processes in agitated vessels.

Representative shear rate

Shear rate and stress rate in an agitated vessel are essential factors, especially for particulate processes and bioprocesses. Sánchez Pérez et al.[54] pointed out the significance of shear rate: (1) shear rate directly affects the apparent viscosity of the non-Newtonian fluid and consequently influences power consumption and other mixing properties; (2) biological substance and suspended solid particles may be damaged or form agglomerates due to the shear rate. Therefore, estimation of the representative shear rate is essential in the design and operation of solid-liquid processes.

Many different equations for the representative shear rate have been proposed. Table 1.1 summarized the reported representative shear rate correlated with the rotational speed of the impeller or power consumption, where all of them were empirically obtained. The most common equation in Table 1.1 is the one proposed by Metzner and Otto,[55] which suggests the representative shear rate in the vessel is proportional to the rotational speed of the impeller. This concept is widely accepted in processes dealing with non-Newtonian fluids so that researchers have provided the proportional constant for different impellers.[56–59]

Material deposition

In crystallization and mining processes, a hard deposit, called scale, attached to the wall shown in Figure 1.3 is a significant issue since scale increases cleaning costs and reduces production capacity. Moreover, scale hazards the health of operators and may damage the equipment in the vessel. A

Table 1.1: Correlation equations for shear rate in the agitated vessel.

Equation	Investigators
$\dot{\gamma} = k_i N$	Metzner and Otto[55]
$\dot{\gamma} = k_i \left(\dfrac{4n}{3n+1} \right)^{n/(n-1)} N$	Calderbank and Moo-Young[60]
$\dot{\gamma} = 4.2N \left(\dfrac{d}{D} \right)^{0.3} \dfrac{d}{b}$	Bowen[61]
$\dot{\gamma} = \dfrac{0.367}{\mu} \left\{ \dfrac{P}{V} \left(\dfrac{V}{V_s N_p} \right)^{0.42} \right\}^{0.55}$	Hoffmann et al.[62]

Figure 1.3: Example of scale formation in a mineral processing plant (a) neutralisation tank, (b) scale grown on its walls, from the paper by Davoody et al.[63]

commonly used strategy to prevent scaling is adding chemical antiscalants suppressing the growth of a scale layer, and promoting the dissolution of the deposition. On the other hand, the industrial application of antiscalants is strongly based on empiricism because the efficiency of antiscalants relies on the type of chemical reaction. One of the other approaches to overcome the scale issue is to control the hydrodynamic flow in the reactor. Hoang,[64] Walker and Sheikholeslami[65] and many other researchers had investigated the hydrodynamic effects on scale formation and showed velocity in the reactor had an important role in suppression of scale growth.

Just suspended speed of the impeller

The efficiency of solid-liquid mass transfer around particles strongly depends on available surface area and hydrodynamic conditions performed by the impeller. Mass transfer around particles is typically promoted the most in the completely suspended condition. However, solid particles tend to settle to the vessel bottom since the density of particles is often larger than that of the liquid in a vessel. Thus, particles should be suspended to enhance mass transfer between liquid and solid phases by agitation.

Zwietering[66] measured the critical rotational speed of different impellers n_{js} when particles moved freely in the vessel without sedimentation at the bottom, called the just suspended speed. Also, Zwietering provided the well-known correlation equation of n_{js} for standard baffled vessels, Equation (1.23), which was recently modified by Kamei et al.[67]

$$n_{\mathrm{js}} = S\nu^{0.1}d_{\mathrm{p}}^{0.2}\left(g\frac{\rho_{\mathrm{p}} - \rho}{\rho}\right)^{0.45}\phi^{0.13}D^{-0.85} \qquad (1.23)$$

Coefficient S depends on the geometric configuration of the vessel. Many other researchers have shown that this correlation equation effectively estimates n_{js} for various systems.

1.3 Objectives

The present dissertation is devoted to resolving two issues in practical solid-liquid processes using agitated vessels and providing beneficial guidelines to design processes and geometrical configuration of the equipment. One issue

is the need for the representative shear rate in an agitated vessel to describe the agglomeration process effectively. The spatial distribution of the shear rate in a vessel leads to difficulty assessing the agglomeration behavior of suspended particles. Therefore, the present work proposed a new representative shear rate which took the shear history into account, and investigated the applicability of the offered shear rate using a simplified model of agglomeration.

Another issue is scaling on the vessel wall. Although the scaling is a complex phenomenon including momentum, heat and mass transfer near the vessel wall, the discussion in previous studies had been limited in the velocity magnitude near the wall. Therefore, in the approach of controlling the hydrodynamics, transport phenomena near the vessel wall must be investigated in detail to understand and suppress scaling on the wall. The present study numerically investigated transport phenomena near the wall of the vessel with a modified baffle configuration. Accordingly, the effect of baffle modification was experimentally qualified.

1.4   Outline of contents

The present thesis is divided into the following sections as shown in Figure 1.4.

Chapter 1 provided the general introduction about agitated vessels. The main focus of this work is the solid-liquid process in agitated vessels, especially agglomeration and scaling processes.

Chapter 2 proposed a new definition of a representative shear rate and

15
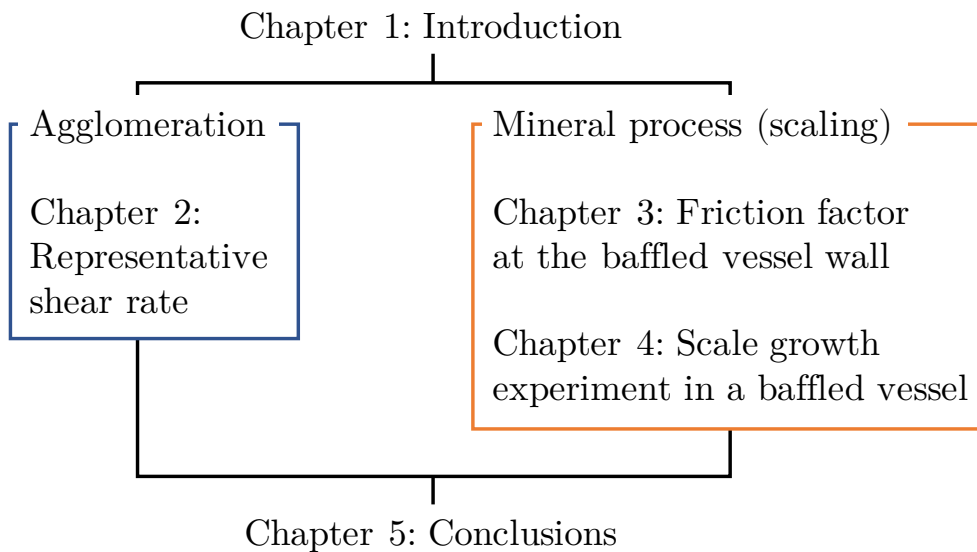
Figure 1.4: Thesis organization.

investigated an agglomeration process in the vessel agitated by a Rushton turbine. The applicability of the proposed shear rate was discussed with a simplified model of the agglomeration behavior of solid particles.

Chapter 3 numerically analyzed the transport phenomena at the sidewall of the agitated vessel in the turbulent regime. A turbulent model was validated with the theoretical values in a non-baffled vessel equipped with a paddle impeller. The friction factors at the wall were compared between the cases with and without baffle clearance. The effect of the installation baffle clearance on practical processes was discussed based on the analogy between momentum, heat, and mass transfer.

Chapter 4, as a verification of the consequence in chapter 3, investigated the effect of the configuration of baffles in a practical process having the issue of material deposition on the wall of the tank. The amount of scale

on the wall was experimentally quantified. Subsequently, the effect of the configuration of baffles was discussed with the velocity distribution in the vessel obtained by numerical calculations.

Chapter 5 gave conclusive remarks of chapters 2–4 and suggested some potential future works.

Nomenclature

A	=	coefficient defined by Equation (1.2) [—]
b	=	height of impeller [m]
B	=	coefficient defined by Equation (1.3) [—]
B_{W}	=	width of baffle [m]
C_{L}	=	coefficient defined by Equation (1.10) [—]
C_{t}	=	coefficient defined by Equation (1.11) [—]
C_{tr}	=	coefficient defined by Equation (1.12) [—]
d	=	diameter of impeller [m]
d_{p}	=	diameter of particle [m]
D	=	diameter of tank [m]
f	=	friction factor defined by Equation (1.7) [—]
f_{∞}	=	asymptotic value of f when $Re_{\mathrm{d}} \to \infty$ [—]
g	=	gravitational acceleration [—]
H	=	height of liquid in the tank [m]
k_{i}	=	constant [—]
K	=	coefficient in Equation (1.22) [—]
m	=	coefficient defined by Equation (1.13) [—]
n	=	flow index [—]
n_{B}	=	the number of baffle plate [—]
n_{p}	=	the number of impeller blade [—]
N	=	impeller rotational speed [s^{-1}]
N_{p}	=	power number [—]
N_{p0}	=	power number at non-baffled condition [—]

$N_\mathrm{p,max}$ = power number at fully baffled condition [—]

Nu = Nusselt number [—]

p = coefficient defined by Equation (1.4) [—]

P = power consumption [W]

Pr = Prandtl number [—]

Re_c = critical Reynolds number [—]

Re_d = impeller Reynolds number [—]

Re_G = modified Reynolds number defined by Equation (1.8) [—]

S = coefficient in Equation (1.23)

t_M = mixing time [s]

V = liquid volume [m^3]

V_s = volume swept by the impeller [m^3]

x = coefficient defined by Equation (1.20) [—]

X = coefficient defined by Equation (1.15) [—]

Greek letters

β = coefficient defined by Equation (1.16) [—]

γ = coefficient defined by Equation (1.17) [—]

$\dot{\gamma}$ = averaged shear rate [s^{-1}]

η = coefficient defined by Equation (1.18) [—]

μ = liquid viscosity [Pa $\cdot$ s]

μ_w = liquid viscosity at vessel wall temperature [Pa $\cdot$ s]

ν = kinetic viscosity [m^2 s^{-1}]

θ = angle of impeller blade [—]

ρ = liquid density [kg m^{-3}]

ρ_p = particle density $[\mathrm{kg\,m^{-3}}]$

ϕ = weight percent of suspended solids to liquid [wt%]

References

(1) Ohmura, N.; Kitamoto, K.; Yano, T.; Kataoka, K. "Novel Operating Method for Controlling Latex Particle Size Distribution in Emulsion Polymerization of Vinyl Acetate," *Industrial & Engineering Chemistry Research* **2001**, *40*, 5177–5183.

(2) Ghobadi, N.; Ogino, C.; Yamabe, K.; Ohmura, N. "Characterizations of the submerged fermentation of Aspergillus oryzae using a Fullzone impeller in a stirred tank bioreactor," *Journal of Bioscience and Bioengineering* **2017**, *123*, 101–108.

(3) Nagata, S.; Yamamoto, K.; Yokoyama, T.; Shiga, S. "Empirical Equations for the Power Requirement of Mixing Impellers, Having a Wide Range of Applicability," *Kagaku Kogaku* **1957**, *21*, 708–715.

(4) Hiraoka, S.; Ito, R. "ON THE RELATION OF POWER INPUT AND TRANSPORT PHENOMENA AT THE WALL OF AGITATED VESSELS," *Journal of Chemical Engineering of Japan* **1974**, *6*, 464–467.

(5) Kamei, N.; Hiraoka, S.; Kato, Y.; Tada, Y.; Shida, H.; Lee, Y.-S.; Yamaguchi, T.; Koh, S.-T. "Power Correlation for Paddle Impellers in Spherical and Cylindrical Agitated Vessels," *Kagaku Kogaku Ronbunshu* **1995**, *21*, 41–48.

(6) Kamei, N.; Hiraoka, S.; Kato, Y.; Tada, Y.; Iwata, K.; Murai, K.; Lee, Y.-S.; Yamaguchi, T.; Koh, S.-T. "Effects of Impeller and Baffle Dimensions on Power Consumption under Turbulent Flow in an Agitated

Vessel with Paddle Impeller," *Kagaku Kogaku Ronbunshu* **1996**, *22*, 249–256.

(7)   Hiraoka, S.; Kamei, N.; Kato, Y.; Tada, Y.; Cheon, H.-G.; Yamaguchi, T. "Power Correlation for Pitched Blade Paddle Impeller in Agitated Vessels With and Without Baffles," *Kagaku Kogaku Ronbunshu* **1997**, *23*, 969–975.

(8)   Kato, Y.; Tada, Y.; Takeda, Y.; Hirai, Y.; Nagatsu, Y. "Correlation of Power Consumption for Propeller and Pfaudler Type Impellers," *Journal of Chemical Engineering of Japan* **2009**, *42*, 6–9.

(9)   Kato, Y.; Obata, A.; Kato, T.; Furukawa, H.; Tada, Y. "Power Consumption of Two-Blade Wide Paddle Impellers," *Kagaku Kogaku Ronbunshu* **2012**, *38*, 139–143.

(10) Ascanio, G. "Mixing time in stirred vessels: A review of experimental techniques," *Chinese Journal of Chemical Engineering* **2015**, *23*, 1065–1076.

(11) Kamiwano, M.; Yamamoto, K.; Nagata, S. "Mixing Performance of Various Agitators," *Kagaku Kogaku* **1967**, *31*, 365–372, a1.

(12) Grenville, R. K.; Nienow, A. W. In *Handbook of Industrial Mixing*; John Wiley & Sons, Ltd: 2003; Chapter 9, pp 507–542.

(13) Mizushina, T.; Ito, R.; Hiraoka, S.; Watanabe, J. "Uniformalization of Temperature Field in Agitated Reactors." *Kagaku Kogaku* **1970**, *34*, 1205–1212.

(14) Takahashi, K.; Sugawara, N.; Takahata, Y. "Mixing Time in an Agitated Vessel Equipped with Large Impeller," *Journal of Chemical Engineering of Japan* **2015**, *48*, 513–517.

(15) Skelland, A. H. P.; Dimmick, G. R. "Heat Transfer Between Coils and Non-Newtonian Fluids with Propeller Agitation," *Industrial & Engineering Chemistry Process Design and Development* **1969**, *8*, 267–274.

(16) Pimenta, T. A.; Campos, J. B. L. M. "Heat transfer coefficients from Newtonian and non-Newtonian fluids flowing in laminar regime in a helical coil," *International Journal of Heat and Mass Transfer* **2013**, *58*, 676–690.

(17) Prada, R. J.; Nunhez, J. R. "Numerical prediction of a nusselt number equation for stirred tanks with helical coils," *AIChE Journal* **2017**, *63*, 3912–3924.

(18) Calderbank, P.; Moo-Young, M. "The continuous phase heat and mass-transfer properties of dispersions," *Chemical Engineering Science* **1961**, *16*, 39–54.

(19) Sano, Y.; Usui, H.; Nishimura, T.; Saito, E. "Correlation of Heat Transfer at the Wall of Mixing Vessel," *Kagaku Kogaku Ronbunshu* **1978**, *4*, 159–165.

(20) Triveni, B.; Vishwanadham, B.; Venkateshwar, S. "Studies on heat transfer to Newtonian and non-Newtonian fluids in agitated vessel," *Heat and Mass Transfer* **2008**, *44*, 1281–1288.

(21) Marui, M.; Tokanai, H. "The Effect of Large Particle Addition on Heat Transfer from Side Wall in Turbulent Agitation Vessel," *Kagaku Kogaku Ronbunshu* **2021**, *47*, 21–95.

(22) Shinji, N., "Mixing: Principles and Applications," A Halsled Press book; Kodansha: 1975.

(23) Nagata, S.; M.Nishikawa; Takimoto, T.; Kita, F.; Kayama, T. "Jacket Side Heat Transfer Coefficient in Mixing Vessel," *Kagaku Kogaku* **1971**, *35*, 924–932, a1.

(24) Bourne, J.; Buerli, M.; Regenass, W. "Heat transfer and power measurements in stirred tanks using heat flow calorimetry," *Chemical Engineering Science* **1981**, *36*, 347–354.

(25) Kobashi, T.; Takahashi, T.; Kitamura, Y. "Heat Transfer Coefficient in Agitated Vessel with Perforated Screw Mixer," *Kagaku Kogaku Ronbunshu* **1990**, *16*, 46–50.

(26) Jo, H. J.; Kim, Y. J.; Hwang, W. R. "Enhancement of mixing performance with anchor-type impellers via chaotic advection," *Chemical Engineering Science* **2021**, *243*, 116757.

(27) Kuncewicz, C.; Szulc, K.; Kurasinski, T. "Hydrodynamics of the tank with a screw impeller," *Chemical Engineering and Processing: Process Intensification* **2005**, *44*, 766–774.

(28) Sanjuan-Galindo, R.; Heniche, M.; Ascanio, G.; Tanguy, P. A. "CFD investigation of new helical ribbon mixers bottom shapes to improve pumping," *Asia-Pacific Journal of Chemical Engineering* **2011**, *6*, 181–193.

(29)   Robinson, M.; Cleary, P. W. "Flow and mixing performance in helical ribbon mixers," *Chemical Engineering Science* **2012**, *84*, 382–398.

(30)   Kuratsu, M.; Nishimi, H.; Mishima, M.; Kamota, T. "New Type Mixing Vessel "MAXBLEND"," *Sumitomo Heavy Industries Technical Report* **1987**, *35*, 74–78.

(31)   Iranshahi, A.; Devals, C.; Heniche, M.; Fradette, L.; Tanguy, P. A.; Takenaka, K. "Hydrodynamics characterization of the Maxblend impeller," *Chemical Engineering Science* **2007**, *62*, 3641–3653.

(32)   Fradette, L.; Thomé, G.; Tanguy, P.; Takenaka, K. "Power and Mixing Time Study Involving a Maxblend® Impeller with Viscous Newtonian and Non-Newtonian Fluids," *Chemical Engineering Research and Design* **2007**, *85*, 1514–1523.

(33)   Hidalgo-Millán, A.; Zenit, R.; Palacios, C.; Yatomi, R.; Horiguchi, H.; Tanguy, P.; Ascanio, G. "On the hydrodynamics characterization of the straight Maxblend® impeller with Newtonian fluids," *Chemical Engineering Research and Design* **2012**, *90*, 1117–1128.

(34)   Mancilla, E.; Yatomi, R.; Zenit, R.; Ascanio, G. "Hydrodynamic Characterization of Three Axial Impellers under Gassed and Ungassed Conditions," *Journal of Chemical Engineering of Japan* **2016**, *49*, 894–903.

(35)   Fontaine, A.; Guntzburger, Y.; Bertrand, F.; Fradette, L.; Heuzey, M.-C. "Experimental investigation of the flow dynamics of rheologically complex fluids in a Maxblend impeller system using PIV," *Chemical Engineering Research and Design* **2013**, *91*, 7–17.

(36) Patel, D.; Ein-Mozaffari, F.; Mehrvar, M. "Using tomography to visualize the continuous-flow mixing of biopolymer solutions inside a stirred tank reactor," *Chemical Engineering Journal* **2014**, *239*, 257–273.

(37) Yatomi, R.; Takenaka, K.; Takahashi, K.; Tanguy, P. A. "Mass Transfer Characteristics by Surface Aeration of Large Paddle Impeller: Application to a Polymerization Reactor with Liquid Level Change," *Journal of Chemical Engineering of Japan* **2007**, *40*, 393–397.

(38) Takahashi, K.; Tanimoto, I.; Sekine, H.; Takahata, Y. "Gas Dispersion in an Agitated Vessel Equipped with Large Impeller," *Journal of Chemical Engineering of Japan* **2014**, *47*, 717–721.

(39) Hiruta, O.; Yamamura, K.; Takebe, H.; Futamura, T.; Iinuma, K.; Tanaka, H. "Application of Maxblend Fermentor® for microbial processes," *Journal of Fermentation and Bioengineering* **1997**, *83*, 79–86.

(40) Saito, I.; Honda, H.; Kawabe, T.; Mukumoto, F.; Shimizu, M.; Kobayashi, T. "Comparison of biotin production by recombinant Sphingomonas sp. under various agitation conditions," *Biochemical Engineering Journal* **2000**, *5*, 129–136.

(41) Ghobadi, N.; Ogino, C.; Ohmura, N. "Intensifying the Fermentation of it Aspergillus oryzae in a Stirred Bioreactor Using Maxblend Impeller," *The Open Chemical Engineering Journal* **2016**, *10*, 88–109.

(42) Minami, T. "Guideline of the design of mixing tank reactors (in Japanese)," *Kagaku Kogaku* **2017**, *81*, 357–360.

(43)   Khazam, O.; Kresta, S. M. "Mechanisms of solids drawdown in stirred tanks," *The Canadian Journal of Chemical Engineering* **2008**, *86*, 622–634.

(44)   Atibeni, R.; Gao, Z.; Bao, Y. "Effect of baffles on fluid flow field in stirred tank with floating particles by using PIV," *The Canadian Journal of Chemical Engineering* **2013**, *91*, 570–578.

(45)   Kato, Y.; Hiraoka, S.; Tada, Y.; Ohnishi, M.; Naganawa, T.; Yamauchi, R.; Shiobara, K. "Mixing Performance of an Agitated Vessel with Bottom Baffles," *Journal of Chemical Engineering of Japan* **2002**, *35*, 208–210.

(46)   Major-Godlewska, M.; Karcz, J. "An effect of the tubular baffles configuration in an agitated vessel with a high-speed impeller on the power consumption," *Chemical Papers* **2018**, *72*, 2933–2943.

(47)   Kato, Y.; Tada, Y.; Takeda, Y.; Atsumi, N.; Nagatsu, Y. "Prediction of Mixing Pattern by Using Power Number Diagram in Baffled and Unbaffled Mixing Vessels," *Journal of Chemical Engineering of Japan* **2010**, *43*, 46–51.

(48)   Wang, S.; Wu, J.; Bong, E. "Reduced IMRs in a mixing tank via agitation improvement," *Chemical Engineering Research and Design* **2013**, *91*, 1009–1017.

(49)   Inoue, Y.; Kato, Y.; Osaka, R.; Natami, K.; Onyango, O. L.; Kawamata, M.; Hashimoto, S. "Enhancement of Fluid Mixing by Deformations of Streak Surface," *Kagaku Kogaku Ronbunshu* **2012**, *38*, 191–202.

(50) Kato, Y.; Kamei, N.; Tada, Y.; Nakaoka, A.; Ibuki, T.; Nagatsu, Y.; Koh, S.-T.; Lee, Y.-S. "Effect of Baffle Length on Power Consumption in Turbulent Mixing Vessel," *Kagaku Kogaku Ronbunshu* **2011**, *37*, 377–380.

(51) Furukawa, H.; Ohtani, S.; Kato, Y.; Tada, Y. "Effects of Location of Baffle and Clearance between Baffle and Vessel Wall on Isolated Mixing Regions," *Journal of Chemical Engineering of Japan* **2018**, *51*, 29–32.

(52) Furukawa, H.; Mizuno, Y.; Kato, Y. "Mixing Performance of Baffles in Shear-Thinning Fluids," *Chemical Engineering & Technology* **2021**, *44*, 1440–1446.

(53) Kondo, S.; Takahashi, K.; Ishida, K.; Kinoshita, K. "Dispersion of Solid Particles in a Vessel Stirred with Dual Impellers," *Kagaku Kogaku Ronbunshu* **2006**, *32*, 387–394.

(54) Sánchez Pérez, J.; Rodríguez Porcel, E.; Casas López, J.; Fernández Sevilla, J.; Chisti, Y. "Shear rate in stirred tank and bubble column bioreactors," *Chemical Engineering Journal* **2006**, *124*, 1–5.

(55) Metzner, A. B.; Otto, R. E. "Agitation of non-Newtonian fluids," *AIChE Journal* **1957**, *3*, 3–10.

(56) AW, N.; TP., E. "Aspects of mixing in rheologically complex fluids," *Chemical Engineering Research and Design* **1988**, *66*, 5–15.

(57) Torrez, C.; André, C. "Power Consumption of a Rushton Turbine Mixing Viscous Newtonian and Shear-thinning Fluids: Comparison between Experimental and Numerical Results," *Chemical Engineering & Technology* **1998**, *21*, 599–604.

(58) Kamei, N.; Hiraoka, S.; Kato, Y.; Tada, Y.; Kuwabara, S.; Lee, Y. S.; Yamaguchi, T.; Koh, S.-T. "Development of Power Correlations for Various Impellers in an Agitated Vessel in Laminar Region Based on a Numerical Analysis of 2-D Flow," *Kagaku Kogaku Ronbunshu* **1994**, *20*, 595–603.

(59) Furukawa, H.; Nakamura, N.; Kato, Y.; Nagumo, R.; Tada, Y. "Metzner-Otto Constant of Paddle Impeller with Two Large Blades in Shear-Thinning Fluid," *Kagaku Kogaku Ronbunshu* **2016**, *42*, 92–95.

(60) Calderbank, P.; Moo-Young, M. "The prediction of power consumption in the agitation of non-Newtonian fluids," *Chemical engineering research and design* **1959**, *37*, 26–33.

(61) Bowen, R. "Unraveling the mysteries of shear-sensitive mixing systems," *Chemical Enginnering* **1986**, *9*, 55–63.

(62) Hoffmann, J.; Büscher, K.; Hempel, D. C. "Determination of maximum shear-stress in stirred vessels (in German)," *Chemie Ingenieur Technik* **1995**, *67*, 210–214.

(63) Davoody, M.; Graham, L. J.; Wu, J.; Witt, P. J.; Madapusi, S.; Parthasarathy, R. "Mitigation of scale formation in unbaffled stirred tanks-experimental assessment and quantification," *Chemical Engineering Research and Design* **2019**, *146*, 11–21.

(64) Hoang, T. A. In *Mineral Scales and Deposits*, Amjad, Z., Demadis, K., Eds.; Elsevier: Amsterdam, 2015, pp 47–83.

(65)   Walker, P.; Sheikholeslami, R. "Assessment of the effect of velocity and residence time in $CaSO_4$ precipitating flow reaction," *Chemical Engineering Science* **2003**, *58*, 3807–3816.

(66)   Zwietering, T. N. "Suspending of solid particles in liquid by agitators," *Chemical Engineering Science* **1958**, *8*, 244–253.

(67)   Kamei, N.; Hiraoka, S.; Furukawa, H.; Kato, Y. "A Discussion of Minimum Rotational Speed for Complete Suspension in Turbulent Solid-Liquid Mixing," *Kagaku Kogaku Ronbunshu* **2022**, *48*, 1–6.

Chapter 2

Representative shear rate for particle agglomeration

2.1 Introduction

Agglomeration of solid particles is a common unit operation in a wide range of solid-liquid processes.[1] Practical applications can be found in the wast water treatment,[2] polymerization[3,4] and production of microalgae.[5] The particle distribution and the shape of agglomerates significantly impacts on the physical properties of the suspension and the operational condition of the process. Furthermore, the product quality is directly affected by the property of suspended agglomerates. It is, therefore, crucial to successfully predict the agglomeration phenomenon and the property of agglomerates.

Generally, three different mechanisms describe the agglomeration of particles. One is the Brownian coagulation which is relevant for small particles. The second one is sedimentation which should be considered for larger par-

ticles colliding due to the difference in the settling velocity.[6] The third one is orthokinetic agglomeration induced by collisions between particles, in the range of 1–40 µm in diameter, in the hydrodynamic flow. The orthokinetic agglomeration can be found in many industrial processes,[7,8] so that it has been theoretically and experimentally investigated for decades. The shear rate is the most significant dominant parameter of the orthokinetic agglomeration since it corresponds to the velocity difference in particles. Smoluchowski[9] proposed a basic mean-field model for the growth of agglomerates in a shear field, and Swift and Friedlander[10] experimentally validated the model. Usui[11] established the thixotropy model considering Brownian and shear forces to estimate the apparent viscosity of suspensions.

The representative shear rate in the flow should be estimated to efficiently predict the orthokinetic agglomeration process. Indeed, theoretical shear rates in some flows had been presented.[12] However, these researches on the representative shear rate for the orthokinetic agglomeration are often limited to the cases in simple flow systems, such as simple shear flow or fully developed turbulent flow, where the spatial shear distribution is homogeneous. However, the conventional agitated vessel, which forms the inhomogeneous shear field, deals with many industrial particulate processes. Consequently, agglomerates in the vessel have shear history, which results in difficulty estimating the representative shear rate. Masuda et al.[13] pointed out that the shear rate for agitated vessels by Metzner and Otto[14] could be an overestimation due to the inhomogeneous shear field in the vessel. Therefore, a new representative shear rate is necessary to describe agglomeration in the agitated vessel.

The present chapter proposes the representative shear rate for agglomeration in the agitated vessel. The agglomeration behavior of particles in the vessel was discussed with this representative shear rate and a simplified agglomeration model.

2.2 Proposal of the representative shear rate

The present work focused on the local residence time of particles to describe the shear history. Figure 2.1 illustrates the conceptual diagram of the proposed representative shear rate. Assuming a micro cube with volume ΔV_i where the shear distribution is homogeneous, particles going through the cube receive the shear force corresponding to the local shear rate $\dot{\gamma}_i$ for the residence time. The representative shear rate was defined as the weighted averaged shear rate of the local residence time as follows.

$$\dot{\gamma}_\tau = \frac{\sum_i \dot{\gamma}_i \Delta V_i \tau_i}{\sum_i \Delta V_i \tau_i} \tag{2.1}$$

where $\tau_i \left(= \sqrt[3]{\Delta V_i}/u_i \right)$ is the local residence time and u_i is the local velocity. $\sum_i$ means the summation in the whole space of the system. Here, particles are assumed to flow on the streamline in the system without the isolated mixing region. This representative shear rate can be regarded as the space-time average of cumulative shear applied to particles in the agglomeration process. On the other hand, the product $\dot{\gamma}_i \tau_i$ can be considered as the shear strain applied to particles in a finite volume which is a reasonable expression for the breakage process reported in the literature.[15,16] This study obtained the local

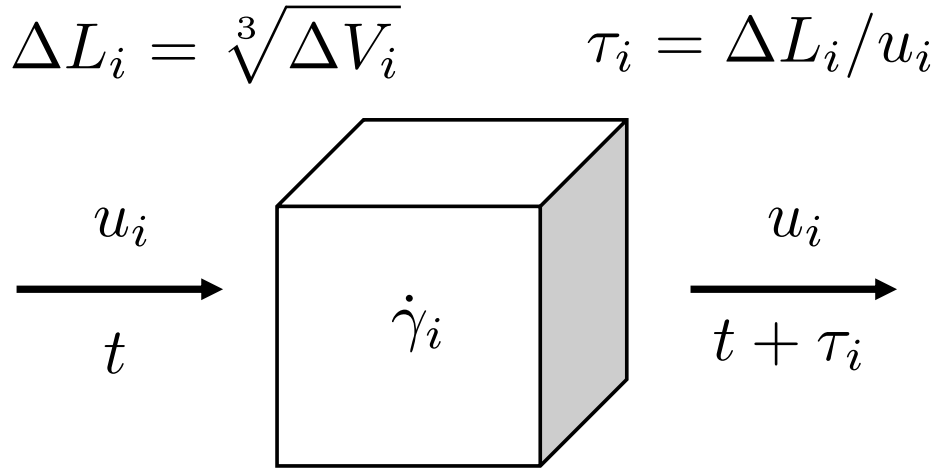$$\Delta L_i = \sqrt[3]{\Delta V_i} \qquad \tau_i = \Delta L_i / u_i$$

Figure 2.1: Conceptual diagram of the weight averaged shear rate based on the local residence time τ_i.

shear rate $\dot{\gamma}_i$ and the local velocity u_i by the CFD calculation, respectively. The volume of the micro cube ΔV_i was defined as the computational cell volume.

2.3 Experimental

This study used polystyrene (PS) spherical particles as model particles, having the average diameter of 4.37 µm and the specific gravity of 1.10, supplied by Sekisui Kasei Co., Ltd. The surface of PS particles is usually charged negatively in the medium, which leads to the repulsion of particles. The electric interaction between PS particles was controlled by adding sodium chloride [NaCl]. The presence of the salt in the suspension increases the ionic strength, and the electric double layer is reduced approximately to the Debye-Hückel length.

The suspension was prepared by dispersing 0.01–1.0wt% of PS particles

in the 68vol% glycerol aqueous solution with the viscosity of $0.028\,\mathrm{Pa\cdot s}$ and the density of $1200\,\mathrm{kg\,m^{-3}}$. Note that the medium was prepared by mixing pure glycerol and NaCl aqueous solution beforehand, and the concentration of NaCl in the suspension was 1.3 M. The suspension was stirred for at least 30 min using a magnetic stirrer after adding PS particles to the medium. Then, the particles were completely dispersed by the homogenizer (T50, IKA-Works Inc.) for 1 h with controlling temperature in a water bath. After homogenization, the suspension was placed in the ultrasonic bath (AS22GTU, AS ONE CORPORATION) for 1 h to break up any agglomerates. All preparation steps were carried out at 24 °C.

Figure 2.2 illustrates the experimental setup for the observation of agglomeration in the agitated vessel. The suspension filled up the flat-bottomed cylindrical vessel having the diameter of 108 mm. The vessel was equipped with a Rushton turbine and the diameter of the impeller was 52 mm. The rotational speed of the impeller was tested in the range of $N = 45\text{--}240\,\mathrm{rpm}$. Accordingly, the Reynolds number was within $Re_\mathrm{d} = 81\text{--}432$.

A small amount of suspension was sampled at the point 3 cm from the liquid surface at a specific time interval. The sample suspension was diluted by distilled water and particle size distribution (PSD) was immediately measured by a laser diffraction particle size analyzer (SALD-300V, SHIMADZU CORPORATION). The particle size analyzer irradiates a laser beam to particles in the suspension and detects the diffraction and scattering light. Different sizes of particles have different patterns of diffraction and scattering light. The device analyzes this optical pattern, then provides the PSD.

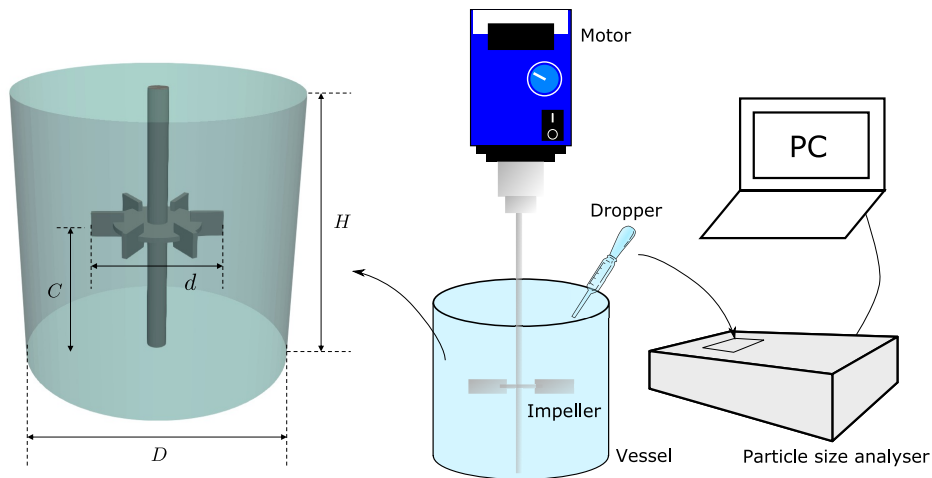The relative magnitude of shear-induced collisions compared to collisions

Figure 2.2: Experimental setup and schematic of the agitated vessel.

by Brownian diffusion and by sedimentation is qualified by the Péclet number Pe and the particle Froude number[17] Fr defined as follows, respectively.

$$Pe = \frac{3\pi\mu\bar{\dot{\gamma}}\xi^3}{4k_{\mathrm{B}}T} \tag{2.2}$$

$$Fr = \frac{Nd}{\sqrt{(s-1)g\xi}} \tag{2.3}$$

where μ is the viscosity of the fluid, $\bar{\dot{\gamma}}$ is the representative shear rate, ξ is the diameter of a particle, k_{B} is the Boltzmann constant, T is the temperature, s is the density ratio of sediment and fluid, and g is the gravitational acceleration.

In this study, Pe was larger than 10^4 even at the lowest representative shear rate, so that the Brownian coagulation was negligible. Also, sedimentation was neglected since Fr was larger than 10^2 at the lowest rotational speed of the impeller. Additionally, the agglomerates can be assumed to follow the flow because the Stokes number for the largest obtained agglomerate

36

was less than 10^{-6}. The Stokes number St was defined as follows.

$$St = \frac{\rho_\mathrm{p} \xi^2 N}{18\mu}$$ (2.4)

2.4   Numerical setup

The flow in the agitated mixing tank was numerically simulated by an open-source CFD software OpenFOAM version 7 to obtain the spatial distribution of the shear rate. This work calculated the steady-state flow of the incompressible Newtonian fluid. The governing equations were the conservation equations and Navier-Stokes equations in a rotating frame as follows.

$$\nabla \cdot \boldsymbol{u}_\mathrm{R} = 0$$ (2.5)

$$(\boldsymbol{u}_\mathrm{R} \cdot \nabla)\boldsymbol{u}_\mathrm{R} + 2\boldsymbol{\Omega} \times \boldsymbol{u}_\mathrm{R} + \boldsymbol{\Omega} \times (\boldsymbol{\Omega} \times \boldsymbol{r}) = -\nabla p + \nu\nabla(\nabla\boldsymbol{u}_\mathrm{R} + (\nabla\boldsymbol{u}_\mathrm{R})^\top) + \boldsymbol{g}$$ (2.6)

where $\boldsymbol{u}_\mathrm{R}$ is the velocity in the rotating frame, $\boldsymbol{\Omega}$ is the angular velocity, $\boldsymbol{r}$ is the position vector, p is the pressure, ν is the kinetic viscosity, and $\boldsymbol{g}$ is the gravitational acceleration in the rotating frame. The existence of particles was neglected to simplify the simulation. The velocity in the inertial frame $\boldsymbol{u}$ can be obtained by the following equation.

$$\boldsymbol{u} = \boldsymbol{u}_\mathrm{R} + \boldsymbol{\Omega} \times \boldsymbol{r}$$ (2.7)

Accordingly, the shear rate $\dot{\gamma}$ is defined by the rate of deformation tensor $\boldsymbol{D}$.

$$\dot{\gamma} = \sqrt{2\boldsymbol{D} : \boldsymbol{D}} \tag{2.8}$$

Here, $\boldsymbol{D}$ is defined as

$$\boldsymbol{D} = \frac{1}{2}(\nabla\boldsymbol{u} + \nabla\boldsymbol{u}^{\top}) \tag{2.9}$$

The multiple reference frames method is often applied to treat the rotational motion in the agitated vessel. This has an advantage to obtain the velocity field in the agitated vessel tank with baffles. In this work, however, the whole computational domain was considered as the rotating frame since the vessel used in the experiment had no baffles. The impeller and the shaft were set as non-slip wall ($\boldsymbol{u}_{\mathrm{R}} = 0$) in the rotating coordinate system. The top surface of the vessel was set as slip wall and the other vessel walls were set as non-slip walls ($\boldsymbol{u} = 0$) in the fixed coordinate system. The computational domain was discretized with hexahedral and tetrahedral grids using cfMesh of a meshing tool. The total number of grids was over 3.8×10^5 and the maximum volume was 1.17×10^{-9} in the tank. The SIMPLE scheme was applied to couple the pressure with the velocity. The relaxation factors for each equation were set as 0.9. The velocity field was regarded to make convergence after the residuals of both velocity in the rotating frame and pressure reached less than 10^{-6}.

2.5 Results and Discussion

2.5.1 Particle agglomeration in the agitated vessel

The present work used the number of particles consisting of each agglomerate defined as the volume ratio of an agglomerate, called agglomerated number A hereafter, to a single particle to describe PSDs. The original PSDs based on volume were obtained by the laser diffraction measurement. Figure 2.3 shows the variation of the median value of the agglomerated numbers A_{50} at each rotational speed of the impeller. The median agglomerated number initially increased as the agglomeration progressed and asymptotically approached a constant value. Considering that agglomeration and breakage co-occur, the balance between these two processes achieved equilibrium when the median agglomerated number reached the constant value. The following exponential type function could describe the temporal change of the median agglomerated number.

$$\frac{A_{50}(t) - A_{50}(\infty)}{A_{50}(0) - A_{50}(\infty)} = \exp(-kt) \tag{2.10}$$

where, $A_{50}(0)$ and $A_{50}(\infty)$ represent initial and stable values of the agglomerated number, respectively, and k is the overall agglomeration rate. Both the stable values of the agglomerated number and the agglomeration rate increased with the higher rotational speed of the impeller corresponding to the higher shear rate except for $N = 45\,\mathrm{rpm}$. This result means that the effect of agglomeration increased more than that of breakage as the increase in shear rate within the experimental condition. Furthermore, the shear effect

39

was not strong enough to break up larger agglomerates. When $N = 45\,\mathrm{rpm}$, the overall agglomeration rate was larger than that in $N = 70\,\mathrm{rpm}$, which implies that the shear rate was so small that breakup rarely occurs when $N = 45\,\mathrm{rpm}$.
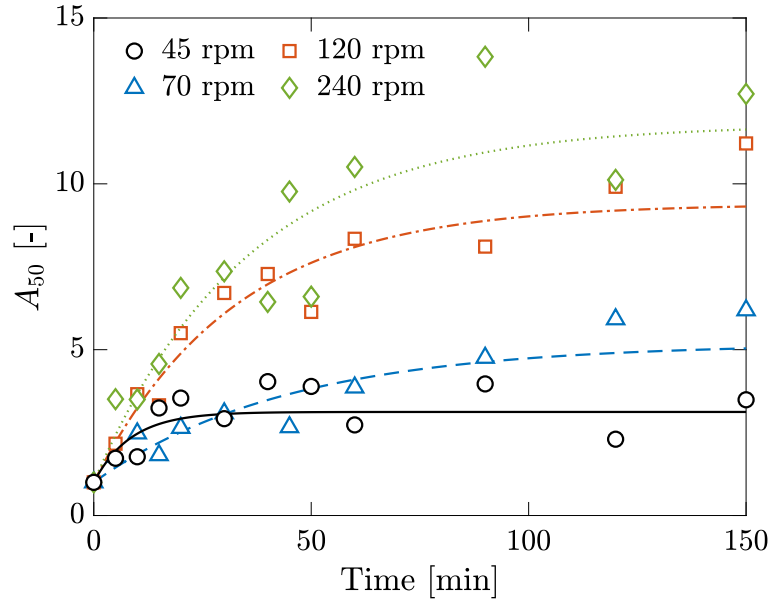

Figure 2.3: Agglomeration process at each rotational speeds of the impeller; curves represent the fitting results by the exponential function in Equation (2.10).

Figure 2.4 shows probability density distributions of the agglomerated number in the steady state at various rotational speeds. This study obtained bimodal PSDs in all of the experimental conditions. Similarly, some previous works reported the formation of bimodal PSDs in the agglomeration process.[18,19] As the first population decreased in time, the second population emerged, representing the formation of agglomerates from single particles. The stable size of yield agglomerates ($A \sim 10.5$) was independent of the rotational speed of the impeller, that is, the shear rate in the vessel. On the
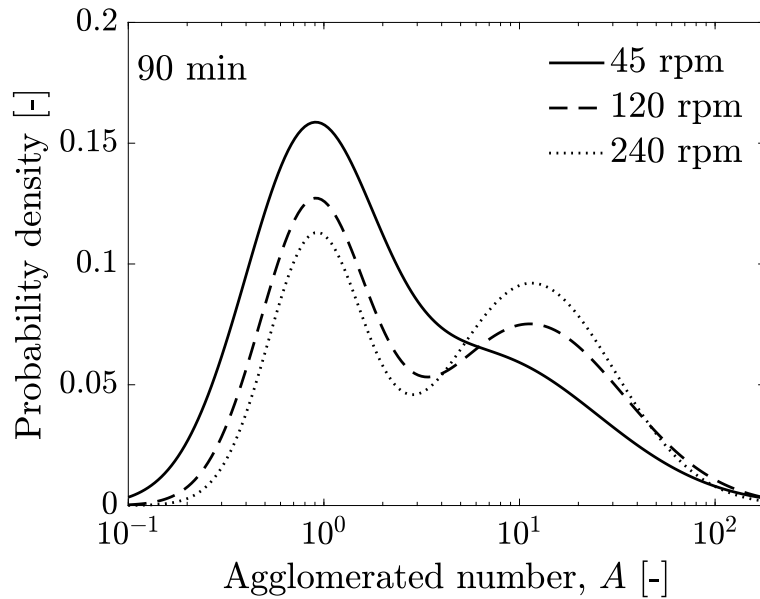
Figure 2.4: Particle size distributions at various rotational speeds of the impeller in the steady-state.

other hand, a larger amount of agglomerates was produced as the increase in rotational speed of the impeller, which resulted in the larger median agglomerated number in higher rotational speed of the impeller as noted in Figure 2.3.

2.5.2 Simplification of the population balance model

The population balance model is one of the most widely used models to describe the evolution of agglomerates, which includes difficulty solving a partial differential equation in terms of time and space. On the other hand, in this work, the population balance model was simplified to an ordinary differential equation, considering that bimodal PSDs were obtained in the experiment. The present subsection presents the simplification process.

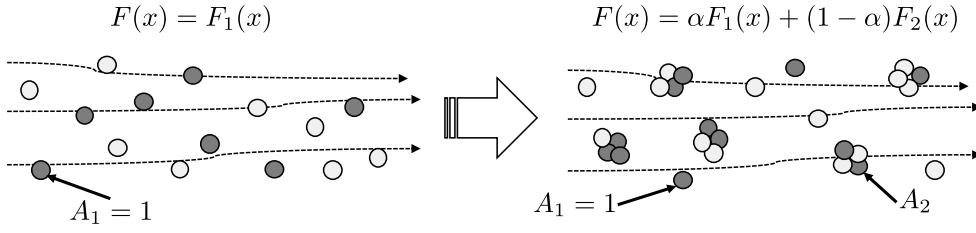Assuming that only two sizes of particles exist in the suspension as shown

Figure 2.5: The agglomeration process providing the bimodel particle size distribution.

in Figure 2.5, the temporal change of the total population of particles n_t is given by the summation of birth and death rates of those two sizes of the particle as follows.

$$\frac{dn_t}{dt} = (B_1 + D_1) + (B_2 + D_2) \tag{2.11}$$

The population of single particles decreases due to the orthokinetic agglomeration, so that, as Smoluchowski[9] proposed, the death rate of single particles D_1 is given by

$$D_1 = -\frac{4}{3}\xi_0^3 \bar{\gamma} n_1^2 \tag{2.12}$$

where ξ_0 is the diameter of single particle, $\bar{\gamma}$ is the representative shear rate, and n_1 is the population of single particles. Then, the population of agglomerates increases by the agglomeration process between single particles. The birth rate of agglomerates is simply expressed as

$$B_2 = -\frac{D_1}{A_2} = \frac{4}{3}\xi_0^3 \bar{\gamma} n_1^2 \frac{1}{A_2} \tag{2.13}$$

where A_2 is the agglomerated number of yeild agglomerates. Several models

42

for the breakage of agglomerates by shear force can be found in the literature, such as the exponential and power-low models.[7,19] The simplification process here defines $\mathcal{B}(=\mathcal{B}(\bar{\dot{\gamma}}))$ as the breakage parameter as a function of the representative shear rate, and expresses the death rate of agglomerates as

$$D_2 = -\mathcal{B}n_2 \tag{2.14}$$

where n_2 is the population of agglomerates. Then the birth rate of single particles can be given by

$$B_1 = -D_2 A_2 = \mathcal{B}n_2 A_2 \tag{2.15}$$

Combining previous equations, Equation (2.11) can be transformed into

$$\frac{\mathrm{d}n_t}{\mathrm{d}t} = -\left(1 - \frac{1}{A_2}\right)\frac{4}{3}\xi_0^3\bar{\dot{\gamma}}n_1^2 + \mathcal{B}(A_2 - 1)n_2 \tag{2.16}$$

With the population ratio of single particle not forming agglomerates to the initial total population, the total population n_t can be rewritten as

$$\begin{aligned}
\frac{n_t}{n_0} &= \frac{n_1 + n_2}{n_0} \\
&= \alpha + \frac{1 - \alpha}{A_2}
\end{aligned} \tag{2.17}$$

where n_0 is the initial total population and α is the agglomeration ratio. Substituting this equation for Equation (2.16), the following differential equation
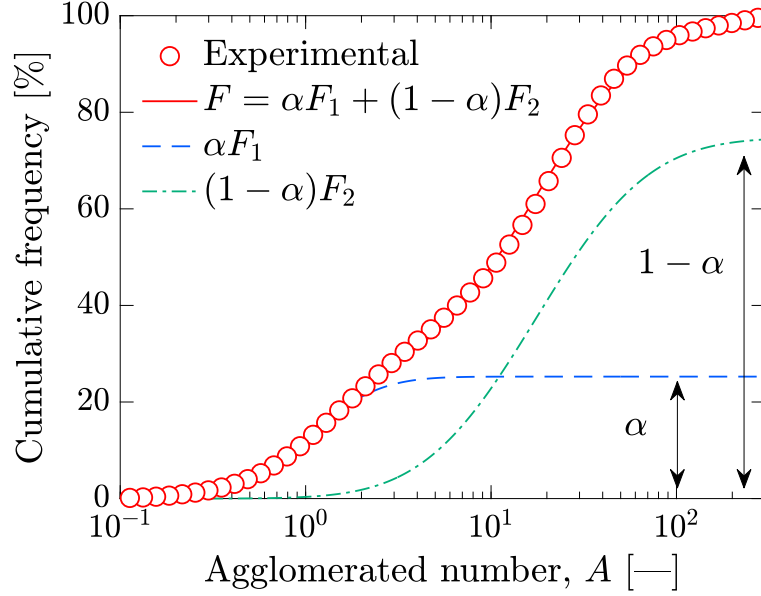
43

Figure 2.6: Cumulative particle size distribution and fitting curves.

in terms of α can be obtained.

$$
\begin{aligned}
\frac{\mathrm{d}\alpha}{\mathrm{d}t} &= -\frac{8}{\pi}\phi_\mathrm{v}\bar{\bar{\gamma}}\alpha^2 + \mathcal{B}(1-\alpha) \\
&= -\mathcal{A}\alpha^2 + \mathcal{B}(1-\alpha)
\end{aligned}
\tag{2.18}
$$

where ϕ_v is the total volume fraction which is constant during the process, and $\mathcal{A}$ is the agglomeration parameter.

The present work obtained α from the PSD in terms of A. The PSD was fitted by the cumulative log-normal mixture distribution function $F(x)$ as shown in Figure 2.6.

$$
F(x) = \alpha F_1(x) + (1-\alpha)F_2(x), \quad 0 \le \alpha \le 1
\tag{2.19}
$$

$$
F_j(x) = \frac{1}{2}\mathrm{erfc}\left(-\frac{\ln x - m_j}{\sigma_j\sqrt{2}}\right), \quad j = 1, 2
\tag{2.20}
$$

44

where m_j and σ_j are constants. As agglomeration processes, α decreases and approaches the stable value.

2.5.3 Effect of rotational speed of the impeller

Figure 2.7 shows the representative shear rate proposed in this work $\dot{\gamma}_\tau$ and two conventional representative shear rates for comparison. One shear rate is the volume-averaged shear rate $\dot{\gamma}_{\text{vol}}$ calculated from the CFD result as

$$\dot{\gamma}_{\text{vol}} = \frac{\sum_i \dot{\gamma}_i \Delta V_i}{\sum_i \Delta V_i} \tag{2.21}$$

Another shear rate $\dot{\gamma}_{\text{m}}$ was proposed by Metzner and Otto[14] as in Table 1.1.

$$\dot{\gamma}_{\text{m}} = k_{\text{m}} \cdot N \tag{2.22}$$

where k_{m} is a proportional constant depending on the impeller. Here, k_{m} is 13.0 for the Rushton turbine.[20] Each representative shear rate increased with the increase in the rotational speed of the impeller. Figure 2.7 indicated that the deviation between the proposed shear rate and the other two became larger with the increase in the rotational speed of the impeller.

In the equilibrium state of the agglomeration process, the left hand of the Equation 2.18 becomes 0. Accordingly, the breakage parameter $\mathcal{B}$ can be calculated as

$$\mathcal{B}(\dot{\gamma}) = \frac{8}{\pi} \phi_{\text{v}} \bar{\dot{\gamma}} \frac{\alpha_{\text{s}}}{1 - \alpha_{\text{s}}} \tag{2.23}$$
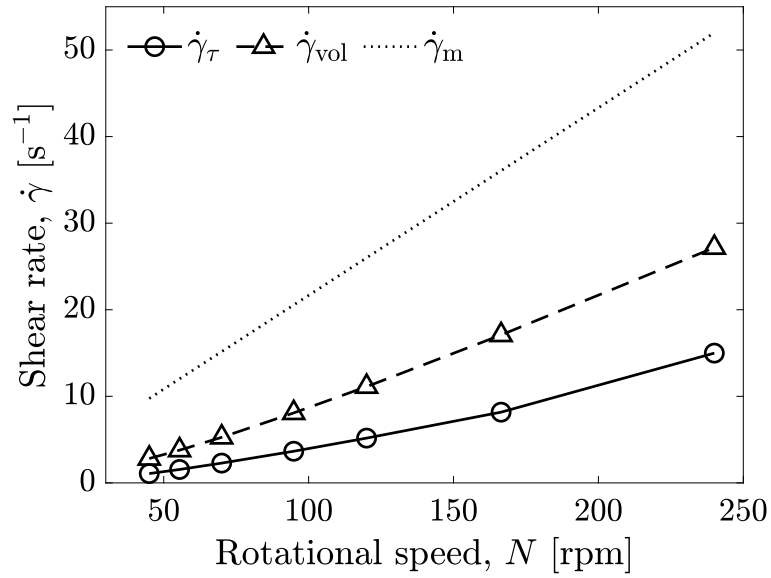
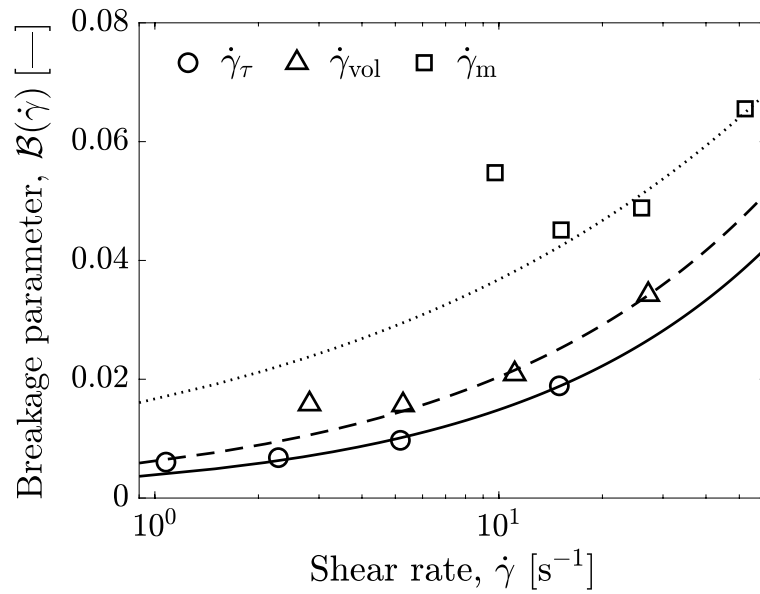Figure 2.7: Effect of the rotational speed of the impeller on representative shear rates.

Figure 2.8: Breakage parameter; curves represent power-law fitting results.
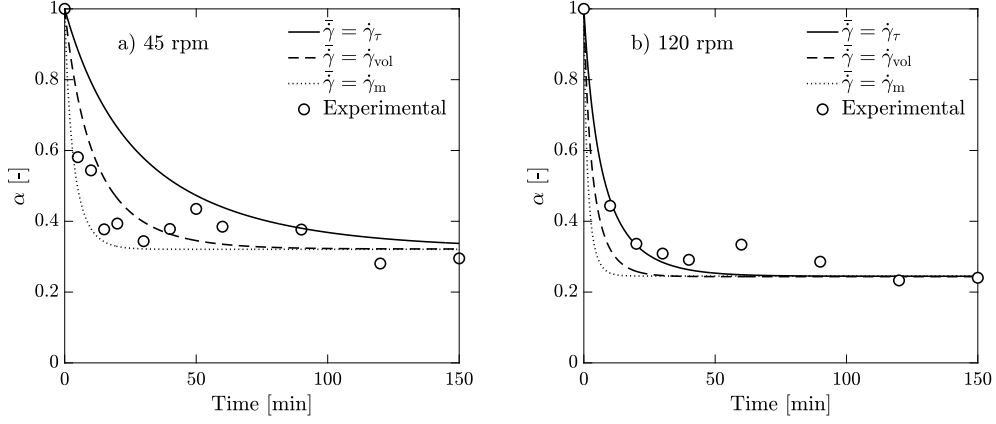
Figure 2.9: Agglomeration processes at (a) $N = 45\,\mathrm{rpm}$, (b) $N = 120\,\mathrm{rpm}$, respectively.

where α_{s} is the stable value of α in the agglomeration experiment. Figure 2.8 plots the breakage parameter for each representative shear rate shown in Figure 2.7, and shows fitting curves using the power-low function. The breakage parameter was successfully described by the power-low model except for $\dot{\gamma}_{\mathrm{m}}$ at $N = 45\,\mathrm{rpm}$.

Figure 2.9 shows the temporal variation of agglomeration ratio for $N = 45,\ 120\,\mathrm{rpm}$, respectively, when the particle concentration was 1.0wt%. Curves represent the prediction results by Equation (2.18), where $\mathcal{A}$ was calculated from the representative shear rate and the experimental condition, and $\mathcal{B}$ was obtained from Figure 2.8. The agglomeration rate, in other words, the rate of decrease in α, was faster when a larger shear rate was applied. It was found that the shear rate estimated by the method of Metzner and Otto was not reasonable for the prediction of particle agglomeration when the particle concentration was 1.0wt% and $N = 120\,\mathrm{rpm}$. This is because this method calculates the shear rate based on the power consumption of the rotating impeller, which only represents the shear rate around the vicinity
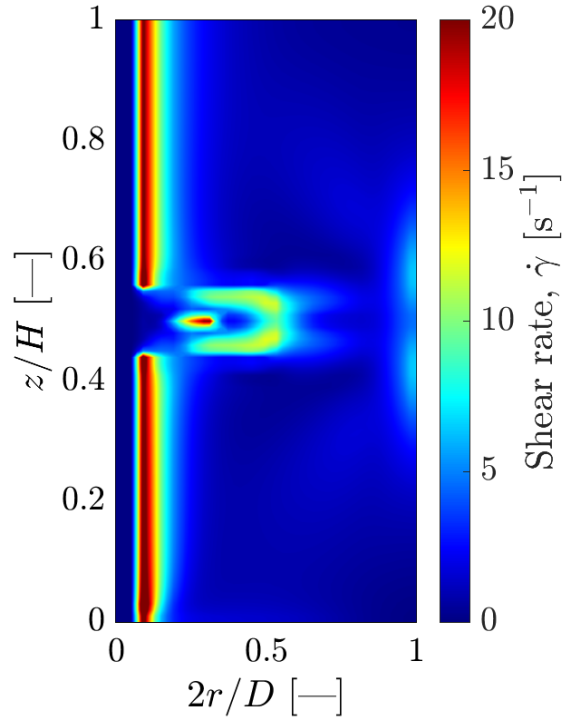
47

Figure 2.10: Shear field in the vessel agitated by the Rushton turbine at $N = 45\,\mathrm{rpm}$.

of the impeller tip, although agglomeration may occur in the whole of the vessel. On the other hand, the proposed representative shear rate considering shear history enabled the most reasonable prediction.

The representative shear rate proposed did not work well when $N = 45\,\mathrm{rpm}$. Rather than that, the other two shear rates were more reasonable for the prediction of the agglomeration process. Considering that there was still a wide distribution of shear rate for $N = 45\,\mathrm{rpm}$ as shown in Figure 2.10, this indicates that most agglomeration occurred around the impeller, and particles or agglomerates just moved around in a distant space away from the rotating impeller.
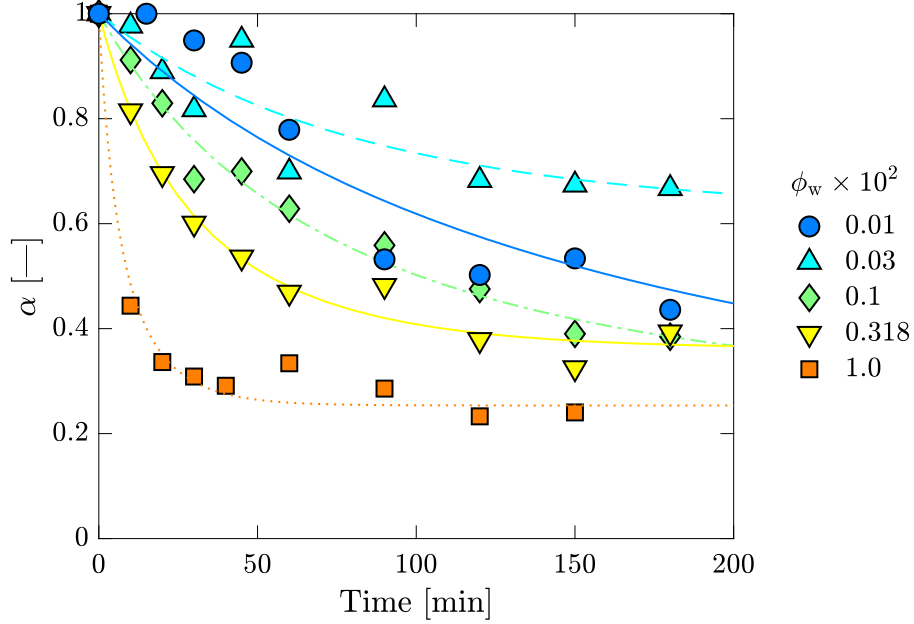
Figure 2.11: Agglomeration process in different particle concentrations at $N = 120\,\mathrm{rpm}$.

2.5.4 Effect of particle concentration

The current subsection presents the results at different particle concentrations at the fixed rotational speed of the impeller $N = 120\,\mathrm{rpm}$ to discuss the applicability of the proposed representative shear rate. The temporal variation of α obtained from the experiment was fitted by the model Equation (2.18). Then, the representative shear rate was estimated from the agglomeration parameter obtained by the fitting as Equation (2.24).

$$\bar{\dot{\gamma}} = \frac{\pi}{8\phi_{\mathrm{v}}}\mathcal{A} \qquad (2.24)$$

Figure 2.11 shows the agglomeration process in terms of the agglomeration rate for different particle concentrations. Curves correspond to the
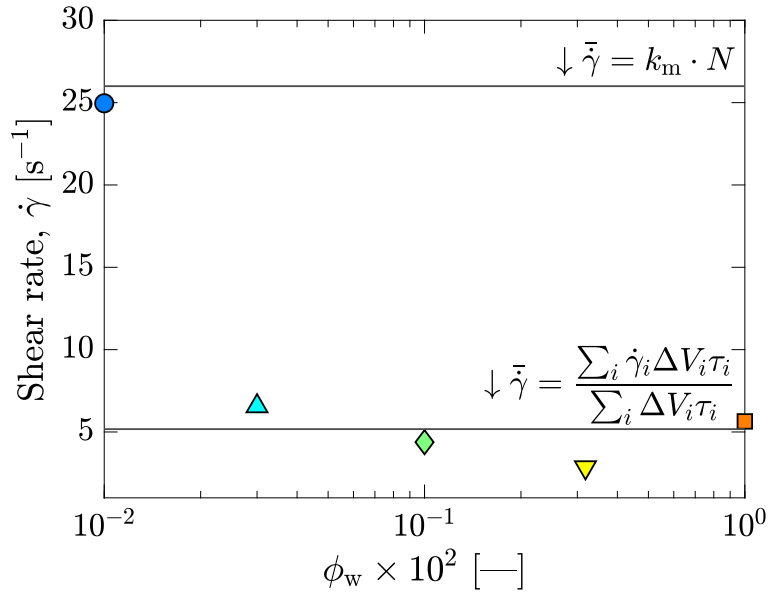
Figure 2.12: Comparison between experimentally estimated shear rate and representative shear rates in different particle concentrations at $N = 120\,\mathrm{rpm}$.

fitting results. The agglomeration rate rapidly decreased, and the agglomeration rate increased with the increase in particle concentration, except for 0.01wt%. This resulted from the increase in the collision frequency by the increase in particle concentration. When the particle concentration was 0.01wt%, the agglomeration slowly progressed in the initial stage. However, the apparent agglomeration rate was faster than that for 0.03%, suggesting that the representative shear rate for the low particle concentration differed from that for other particle concentrations.

Figure 2.12 compares the experimentally estimated shear rate and two representative shear rates, i.e., one proposed in this work and one estimated by the method of Metzner and Otto. Almost the same representative shear rate was obtained when the particle concentration was higher than 0.03wt%,

and the proposed one successfully estimated the representative shear rare for agglomeration in the agitated vessel. On the other hand, a much high shear rate was obtained at the particle concentration was 0.01wt%, which showed a good agreement with the shear rate of Metzner and Otto. These results imply that agglomerates formed around the impeller at the lowest particle concentration since $\dot{\gamma}_m$ represent the shear rate near the rotating impeller. Also, it can be concluded that the local residence time should be taken into account to consider the representative shear rate and design agglomeration process when agglomeration may occur in the whole of the vessel.

2.6   Conclusions

The present chapter proposed the new representative shear rate for agglomeration as the weighted average shear rate of the local residence time. Then, this chapter experimentally investigated the agglomeration process of microscale particles using the Rushton turbine and assessed the applicability of the proposed shear rate. The agglomeration experiment yielded bimodal particle size distributions, and the stable size of produced agglomerate was independent of the rotational speed of the impeller. Accordingly, the agglomeration process was discussed using the ordinary differential equation, which is the simplified population balance equation. The proposed representative shear rate successfully predicted the agglomeration process except for the low rotational speed of the impeller and the low particle concentration. It was concluded that the local residence time should be considered to estimate the representative shear rate in the design of agglomeration processes.

Nomenclature

A $\qquad$ = the number of particles consisting an agglomerate [—]

A_{50} $\qquad$ = median value of A

$\mathcal{A}$ $\qquad$ = agglomeration parameter, $(= 8/(\phi_v \bar{\dot{\gamma}}))$ $[\mathrm{s}^{-1}]$

B_1, B_2 $\qquad$ = birth rate [—]

$\mathcal{B}$ $\qquad$ = breakage parameter $[\mathrm{s}^{-1}]$

C $\qquad$ = clearance between vessel bottom and impeller [m]

d $\qquad$ = diameter of impeller [m]

D $\qquad$ = diameter of vessel [m]

$\boldsymbol{D}$ $\qquad$ = deformation tensor $[\mathrm{s}^{-1}]$

D_1, D_2 $\qquad$ = death rate $[\mathrm{s}^{-1}]$

Fr $\qquad$ = particle Froude number [—]

$g, \boldsymbol{g}$ $\qquad$ = gravitational acceleration [—]

H $\qquad$ = height of liquid in the tank [m]

k $\qquad$ = overall agglomeration rate in Equation (2.10) $[\mathrm{s}^{-1}]$

k_{B} $\qquad$ = Boltzmann constant $[\mathrm{J\,K}^{-1}]$

k_{m} $\qquad$ = constant in Equation (2.22) [—]

ΔL_i $\qquad$ = edge length of the cube with volume ΔV_i [m]

m_j $\qquad$ = parameter in Equation (2.20) [—]

n_0 $\qquad$ = initial population of particles [—]

n_1, n_2 $\qquad$ = population of particles or agglomerates [—]

n_{t} $\qquad$ = total population of particles [—]

N $\qquad$ = rotational speed of the impeller $[\mathrm{s}^{-1}]$

p $\qquad$ = pressure [Pa]

Pe = Péclet number [—]

r = radial coordinate [m]

Re_d = impeller Reynolds number [—]

$\boldsymbol{r}$ = position vector [m]

s = density ratio of sediment and fluid [—]

St = Stokes number [—]

t = time [s]

T = temperature [K]

$\boldsymbol{u}$ = velocity [m s^{-1}]

u_i = local velocity [m s^{-1}]

$\boldsymbol{u}_\mathrm{R}$ = velocity in the rotating frame [m s^{-1}]

ΔV_i = local volume or cell volume in CFD [m^3]

z = axial coordinate [m]

Greek letters

α = agglomeration ratio defined by Equation (2.17) [—]

α_s = α in steady state [—]

$\dot{\gamma}$ = shear rate [s^{-1}]

$\dot{\gamma}_i$ = local shear rate [s^{-1}]

$\dot{\gamma}_\mathrm{m}$ = shear rate proposed by Metzner and Otto as in Equation (2.22) [s^{-1}]

$\dot{\gamma}_\mathrm{vol}$ = volume-averaged shear rate as in Equation (2.21) [s^{-1}]

$\dot{\gamma}_\tau$ = representative shear rate defined in Equation (2.1) [s^{-1}]

$\bar{\dot{\gamma}}$ = representative shear rate [s^{-1}]

μ = liquid viscosity [Pa·s]

ν = kinetic viscosity [m^2 s^{-1}]

ξ = diameter of a particle or an agglomerate [m]

ξ_0 = diameter of a single particle [m]

ρ_{p} = particle density [$\mathrm{kg\,m^{-3}}$]

σ_j = parameter in Equation (2.20) [—]

τ_i = local residence time [s]

ϕ_{v} = volume fraction of particle [—]

ϕ_{w} = weight fraction of particle [—]

$\mathbf{\Omega}$ = angular velocity [$\mathrm{s^{-1}}$]

References

(1) Kusters, K. A.; Wijers, J. G.; Thoenes, D. "Aggregation kinetics of small particles in agitated vessels," *Chemical Engineering Science* **1997**, *52*, 107–121.

(2) Lu, S.; Zhu, K.; Song, W.; Song, G.; Chen, D.; Hayat, T.; Alharbi, N. S.; Chen, C.; Sun, Y. "Impact of water chemistry on surface charge and aggregation of polystyrene microspheres suspensions," *Science of The Total Environment* **2018**, *630*, 951–959.

(3) Vaccaro, A.; Šefčík, J.; Wu, H.; Morbidelli, M.; Bobet, J.; Fringant, C. "Aggregation of concentrated polymer latex in stirred vessels," *AIChE Journal* **2006**, *52*, 2742–2756.

(4) Ueda, T.; Yoshimi, T.; Hurukawa, N. "Process Development of Modifier Resins Based on the Agglomeration Mechanism of Polymer Latex," *Journal of smart processing* **2016**, *5*, 334–341.

(5) Pirwitz, K.; Rihko-Struckmann, L.; Sundmacher, K. "Comparison of flocculation methods for harvesting Dunaliella," *Bioresource Technology* **2015**, *196*, 145–152.

(6) Jiang, Q.; Logan, B. E. "Fractal dimensions of aggregates determined from steady-state size distributions," *Environmental Science & Technology* **1991**, *25*, 2031–2038.

(7) Wang, L.; Marchisio, D.; Vigil, R.; Fox, R. "CFD simulation of aggregation and breakage processes in laminar Taylor-Couette flow," *Journal of Colloid and Interface Science* **2005**, *282*, 380–396.

(8) Selomulya, C.; Bushell, G.; Amal, R.; Waite, T. D. "Aggregation Mechanisms of Latex of Different Particle Sizes in a Controlled Shear Environment," *Langmuir* **2002**, *18*, 1974–1984.

(9) Smoluchowski, M. "Versuch einer mathematischen Theorie der Koagulationskinetik kolloider Lösungen," *Z. physikalische Chemie* **1917**, *92*, 129–168.

(10) Swift, D. L.; Friedlander, S. "The coagulation of hydrosols by brownian motion and laminar shear flow," *Journal of Colloid Science* **1964**, *19*, 621–647.

(11) Usui, H. "Rheological Model for Agglomerative Slurry of Mono-modal Silica Particles," *Kagaku Kogaku Ronbunshu* **1999**, *25*, 459–465.

(12) Zhu, Z. "Theory on Orthokinetic Flocculation of Cohesive Sediment: A Review," *Journal of Geoscience and Environment Protection* **2014**, *02*, 13–23.

(13) Masuda, H.; Tsuda, K.; Matsui, K.; Komoda, Y.; Ohmura, N. "Effect of Shear Rate Distribution on Particle Aggregation in a Stirred Vessel," *Chemical Engineering & Technology* **2017**, *40*, 493–497.

(14) Metzner, A. B.; Otto, R. E. "Agitation of non-Newtonian fluids," *AIChE Journal* **1957**, *3*, 3–10.

(15) Komoda, Y.; Furuse, N.; Hidema, R.; Suzuki, H. "Effect of Additives on the Rapid Destruction Process of Particle Aggregates in a Startup Shear Flow," *Journal of Chemical Engineering of Japan* **2020**, *53*, 422–430.

(16) Olalla, B.; Carrot, C.; Fulchiron, R.; Boudimbou, I.; Peuvrel-disdier, E. "Analysis of the influence of polymer viscosity on the dispersion of magnesium hydroxide in a polyolefin matrix," *Rheologica Acta* **2012**, *51*, 235–247.

(17) Aguirre-Pe, J.; Olivero, M. L.; Moncada, A. T. "Particle Densimetric Froude Number for Estimating Sediment Transport," *Journal of Hydraulic Engineering* **2003**, *129*, 428–437.

(18) Anne-Archard, D.; d'Olce, M.; Tourbin, M.; Frances, C. "Aggregation of silica nanoparticles in concentrated suspensions under turbulent, shear and extensional flows," *Chemical Engineering Science* **2013**, *95*, 184–193.

(19) Tourbin, M.; Frances, C. "Experimental characterization and population balance modelling of the dense silica suspensions aggregation process," *Chemical Engineering Science* **2008**, *63*, 5239–5251.

(20) "Kagaku Kougaku Binran," The Society of Chemical Engineers, J., Ed.; Maruzen: Tokyo, 1999.

Chapter 3

Friction factor distribution at the sidewall of baffled vessels

3.1　Introduction

Scaling on the wall of agitated vessels is a complicated phenomenon, including heat and mass transfer. Chemical reactions leading to a material deposition can be promoted and suppressed by thermal control at the wall of the vessel. The mass transfer at the wall of the vessel and around baffles is also significant since materials often deposit on the place where the mass transfer is poor. According to the Chilton-Colburn analogy in a fully turbulent regime, heat and mass transfer directly relate to momentum transfer, in other words, the friction factor at the wall. Therefore, investigations on transport phenomena near the vessel wall based on the analogy are necessary to suppress scaling.

Literature had reported heat and transfer at the vessel wall. Hiraoka et al.[1] provided a correlation equation of the heat transfer coefficient near the

sidewall of the non-baffled vessel using the friction factor calculated by the power consumption of the impeller, as follows.

$$(h/\rho c_{\mathrm{p}} v_\theta) Pr^{2/3}(1.7d/\beta D) = f/2 \tag{3.1}$$

Shiobara et al.[2] studied the similarity of heat and momentum transfer at the sidewall of the non-baffled vessel and proposed the following correlation equation in the form of j-factor.

$$j_{\mathrm{H}}(md/\beta D) \sim f/2 \tag{3.2}$$

where m is a correlation parameter calculated from the radius of cylindrically rotating zone. On the other hand, many works had been done on mass transfer at the vessel wall and around baffles[3–5] as well as heat transfer. Calderbank and Moo-Young[6] pointed out the slip velocity plays an important role in mass transfer between two phases. Thus, the friction factor, which strongly relates to the slip velocity, is supposed to provide an estimation of the mass transfer coefficient in the same way of Equations (3.1) and (3.2) according to the Chilton-Colburn analogy.

Although works by Hiraoka et al.[1] and Shiobara et al.[2] provided meaningful information on heat transfer, their results are limited to the average value, not to local ones. The local value of the friction factor has been measured along the axial direction on the wall of the non-baffled tank with small impellers.[7–9] However, the local distribution of the friction factor, heat or mass transfer coefficient, is not clarified enough in an agitated vessel equipped with
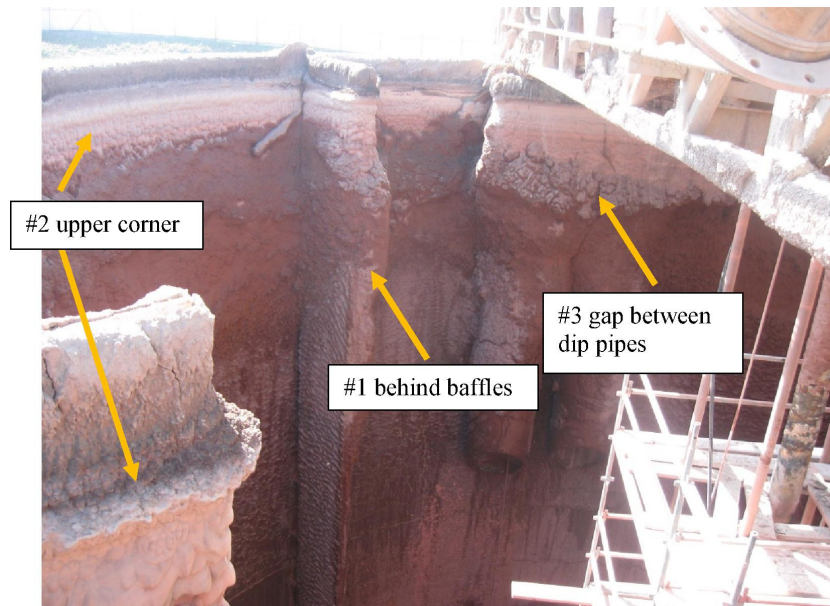
Figure 3.1: A neutralization tank inside view before de-scaling, from the paper by Wu et al.[10]

a large impeller, even though the friction factor must significantly impact the transport phenomena. Especially in baffled tanks, not only the axial but the tangential distribution of the friction factor should be taken into account since baffles make the flow unsymmetrical along the tangential direction and poor mixing regions emerge around them, which results in the undesirable reduction of mass and heat transfer there and hight potential for scaling as shown in Figure 3.1.

The present chapter is devoted to this perspective by numerically studying the local friction factor on the wall of a baffled vessel with a large impeller in the turbulent regime using computational fluid dynamics simulation with the SST k-ω model. Large impellers, the MAXBLEND® impeller here, are typically superior to small impellers in the heat and mass transfer perfor-

60

mance. Consequently, a large impeller is supposed to efficiently reduce the amount of scale. This study focused on the baffle configuration, introducing the clearance between baffles and the vessel wall to strength hydrodynamic flow behind baffles.

In the present chapter, the fluid flow agitated by a paddle impeller was calculated to validate the numerical procedure and obtained velocity near the wall. Then, the friction factor distribution on the sidewall of the vessel with the large impeller was numerically obtained and discussed.

3.2   Numerical setup

Two laboratory-scale stirred tanks with and without baffles were numerically investigated. Agitation was provided by two different impellers, i.e., an eight blade paddle impeller and a MAXBLEND® impeller. The geometrical details of the impeller, tank, and baffles are illustrated in Figure 3.2 and listed in Table 3.1.

Numerical simulations were carried out by a finite volume method using the commercial CFD software R-FLOW. All simulations were performed by solving the continuity and Navier-Stokes equations. The SST k-ω model[11,12] was adopted to investigate the transport phenomena near the wall in the turbulent regime. As an eddy-viscosity model, the SST k-ω model consists of two transport equations for the turbulent kinetic energy k, and for the specific turbulent dissipation rate $\omega (= \varepsilon/k)$. The eddy viscosity μ_t is calculated from the turbulent kinetic energy k and the specific turbulent dissipation rate ω as $\mu_\mathrm{t} = \rho k/\omega$. The SST k-ω model uses a blending function to switch between
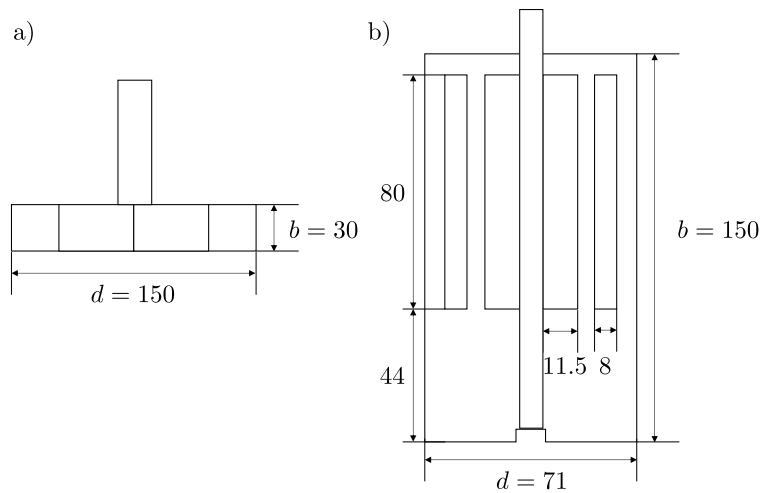
Figure 3.2: Impellers: (a) paddle, and (b) MAXBLEND® (dimensions in millimeters).

the k-ε model in free-stream turbulent flow and the standard k-ω model in the viscous sublayer near the nonslip wall.

The established computational region consists of two domains, i.e., stationary and rotating domains, as shown in Figure 3.3. The stationary domain corresponds to the vessel without baffles for the paddle impeller and with baffles for the MAXBLEND® impeller. On the other hand, the rotational domain does the impeller and the mixing shaft. The diameter of the rotating domain is larger than that of the impeller and does not contact baffles. In addition, the upper surface of it is the same level as the stationary domain, and the lower surface has a slight gap with the tank bottom. Thus, the rotating domain completely contains the impeller and shaft. The velocity in the stationary domain was calculated based on the momentum balance with that in the rotating domain. The rotational domain rotated counterclockwise.

The total number of cells discretized unequal intervals was 6.26×10^5

Table 3.1: Impeller, tank and baffle dimensions

Impeller	Parameter	Value	
Paddle	d	150 ($= 0.5D$)	mm
	b	30 ($= 0.1D$)	mm
	D	300	mm
	H	300 ($= D$)	mm
	n_B	0	–
MAXBLEND®	d	71	mm
	b	130	mm
	D	132.5	mm
	H	150	mm
	n_B	4	–
	B_W	10 ($= 0.075D$)	mm
	B_H	150 ($= H$)	mm
	B_C	0 or 10	mm

in the stationary domain and 9.6×10^{-4} in the rotating one for the paddle impeller ($58 \times 180 \times 60$, $20 \times 240 \times 20$; the radial, azimuthal, and axial directions, respectively). Those for MAXBLEND® impeller were 6.32×10^5 ($31 \times 204 \times 100$) in the stationary domain and 2.12×10^5 ($26 \times 80 \times 102$) in the rotating one, respectively.

In the simulation, the top liquid surface of the tank was regarded as a slip wall, and the other tank walls, baffles, impeller, and shaft surface were set as nonslip walls. The fully turbulent flow of an incompressible Newtonian fluid ($\rho = 1.0 \times 10^{-3}$ kg m^{-3}, $\mu = 1.0 \times 10^{-3}$ Pa·s) was calculated at $Re_\text{d} = 3.0 \times 10^4$ for the paddle impeller, and at $Re_\text{d} = 8.0 \times 10^3$ for the MAXBLEND® impeller.

Steady state simulations were performed to obtain the initial flow velocity for the time dependent calculation by adopting a sufficient number of iterations to guarantee that the residuals of all the velocity components were
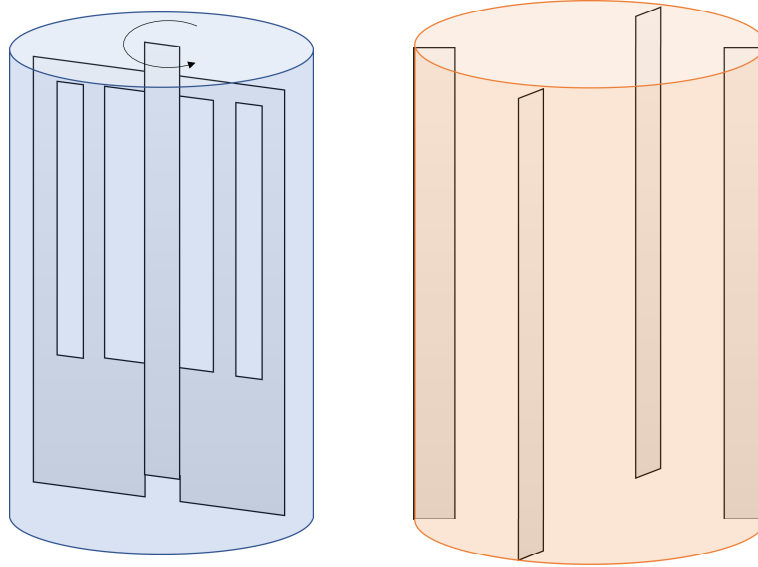
Figure 3.3: Stationary and rotating domains in the CFD simulation; note that a non-baffled tank was used for the paddle impeller.

lower than 9.0×10^{-6}. Then time dependent simulations were carried out with the time step of 1.0×10^{-3} s, where the Courant number was at least lower than 0.7. The present chapter shows the calculation results after over 10 times of impeller rotation.

3.3 Results and Discussion

3.3.1 Validation of calculation model

Although many numerical investigations on the flow in agitated vessels can be found during the development of CFD, few of them focused on the friction factor or the near-wall velocity distribution. In this study, thus, not only the numerically obtained values of bulk velocity were validated by experimental results reported in the literature, but the near-wall velocity distribution was

compared with the theoretical value.

Figure 3.4 shows the comparison of the tangential velocity distribution at different vertical positions for the paddle impeller. The tangential velocity was normalized by the impeller tip velocity U_0. The numerically obtained tangential velocity distribution was not dependent on the vertical position as indicated in the literature.[13,14] It can be also seen that the numerical results in $r > r_d$ agree well with the reported experimental values by Nagata et al.[15] and Yoshida et al.[13] Moreover, the model correctly predicted the linear trend in $r < r_d$, which is typically regarded as rigid body rotation. These results demonstrated the validity of the CFD calculation in the bulk region in the present study.
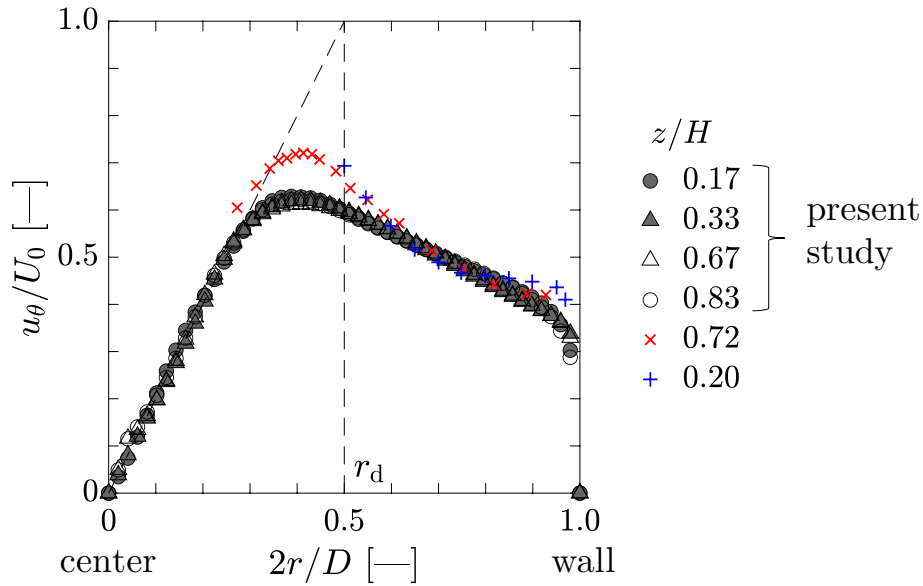
Figure 3.4: Tangential velocity distribution for the paddle impeller, $Re_d = 30000$, ×: Nagata et al.,[15] +: Yoshida et al.[13]

Hiraoka et al.[16] proposed a universal expression of tangential velocity near

65

the sidewall in the non-baffled tank within the turbulent regime for paddle impellers;

$$u^{++} = 5.75 \log y^{++} + 5.5 \quad (20 < y^{++} < 70) \tag{3.3}$$

where

$$u^{++} = u^+ \left(\frac{\beta D}{1.7d} \right), \quad y^{++} = y^+ \left(\frac{\beta D}{1.7d} \right) \tag{3.4}$$

$$u^+ = \frac{u_\theta}{u_w^*}, \quad y^+ = \frac{y u_w^*}{\nu} \tag{3.5}$$

and u_w^* is the friction velocity. In this study, u_w^* was calculated by the normal gradient of the tangential velocity at the sidewall of the tank as follows:

$$u_w^* = \sqrt{\nu \left. \frac{\partial u_\theta}{\partial r} \right|_{\text{wall}}} \tag{3.6}$$

Hiraoka et al. also indicated that u^{++} and y^{++} must satisfy the following relationship near the sidewall, namely, viscous sublayer.

$$u^{++} = y^{++} \tag{3.7}$$

Figure 3.5 shows the numerically obtained non-dimensional tangential velocity profile and model lines. At the viscous sublayer, the velocity profile certainly coincides well with Equation (3.7). In the range of $20 < y^{++}$, a linear trend corresponding to the model can be found in the semilogarithmic scale and the calculated velocity agreed well with the model value. As Tamburini et al.[17] pointed out, at the very high Re_d, eddy-viscosity models
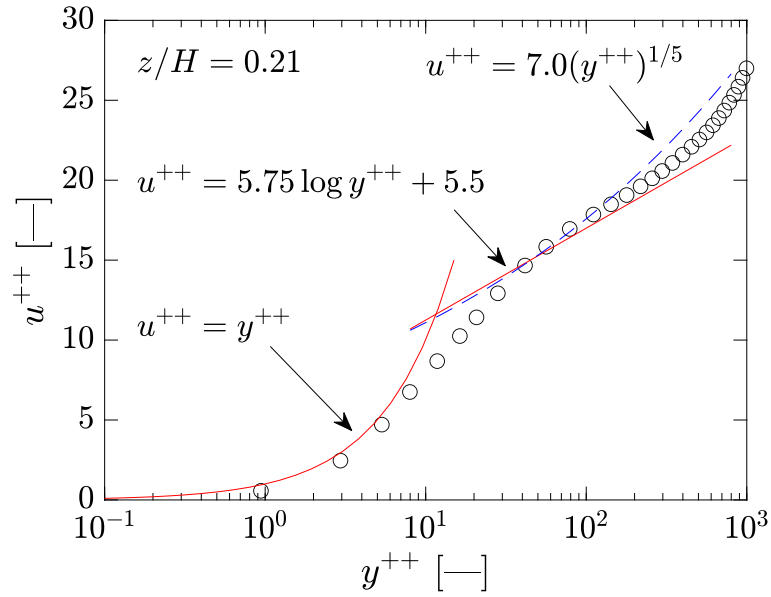
Figure 3.5: Universal tangential velocity distribution for the paddle impeller.

including the SST k-ω model slightly overestimate the power consumption of the impeller due to the turbulence anisotropy. Even though the SST k-ω model provides larger power consumption, Tamburini et al.[17] also concluded that the SST k-ω model was reliable enough to predict the flow in an agitated tank both with and without baffles. The calculation in this study also provided a reasonable estimation so that the the simulation results here were regarded to be validated both at the viscous sublayer and in the range of $20 < y^{++}$.
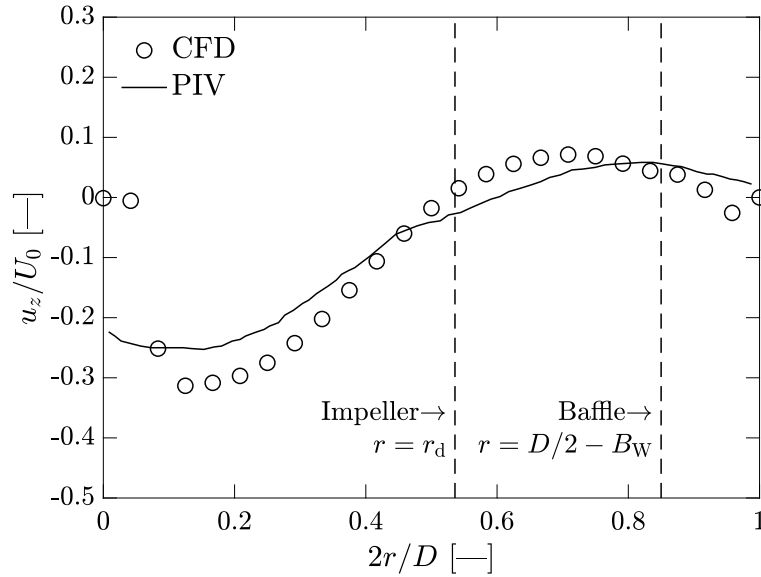
Figure 3.6: Vertical velocity profile for the MAXBLEND® impeller, CFD: this work, PIV: Hidalgo-Millán et al.[18]

3.3.2 Flow fields induced by the MAXBLEND® impeller

Figure 3.6 describes vertical velocity at $z/H = 0.88$ as a function of the radial distance for the MAXBLEND® impeller. Experimental data obtained by particle image velocimetry (PIV) measurement by Hidalgo-Millán et al.[18] were used to validate the numerical results. Dashed lines represent the radial positions of the impeller and the baffle tips. While a downward flow was formed within $r < r_\mathrm{d}$, an upward flow was observed in the range of $r > r_\mathrm{d}$, which can lead to a great mixing performance. This flow pattern can be typically found in the PIV measurement[18] and other experimental works. CFD results show good agreement with the experimental data, which indicates that the numerical results for the MAXBLEND® impeller were reliable.

68

Figure 3.7 shows the comparison of the velocity field in the r-z plane for $\theta = 45°$ in baffled vessels without and with baffle clearance. Numerical results were averaged in a single rotation of the impeller. It can be observed that the flow induced by the impeller paddle moved both upward and downward. Consequently, a vortex flow was formed in the lower part of the vessel regardless of baffle clearance. In addition, a large vortex can be seen in the range of $z/H > 0.4$ in the case without baffle clearance, which is consistent with previous experiments.[18,19] When the clearance was added between the sidewall and baffles, the flow in $z/H > 0.4$ became more complex. The single circulation observed in the vessel without baffle clearance was divided into two circulations. This deformation of the flow pattern by adding baffle clearance may affect the mixing performance so that further investigations are needed for engineering applications.

3.3.3 Effect of baffle clearance on the friction factor

The friction factor for a flat plate in the turbulent regime is defined as

$$f = \frac{\tau_{\mathrm{w}}}{\rho U^2/2} \tag{3.8}$$

where $\tau_{\mathrm{w}} \, (> 0)$ is the shear stress at the wall and U is the velocity at the edge of the turbulent boundary layer. On the other hand, Hiraoka et al.[20] defined the friction factor of an agitated vessel based on the characteristic velocity v_θ in the same manner as Equation (3.8).

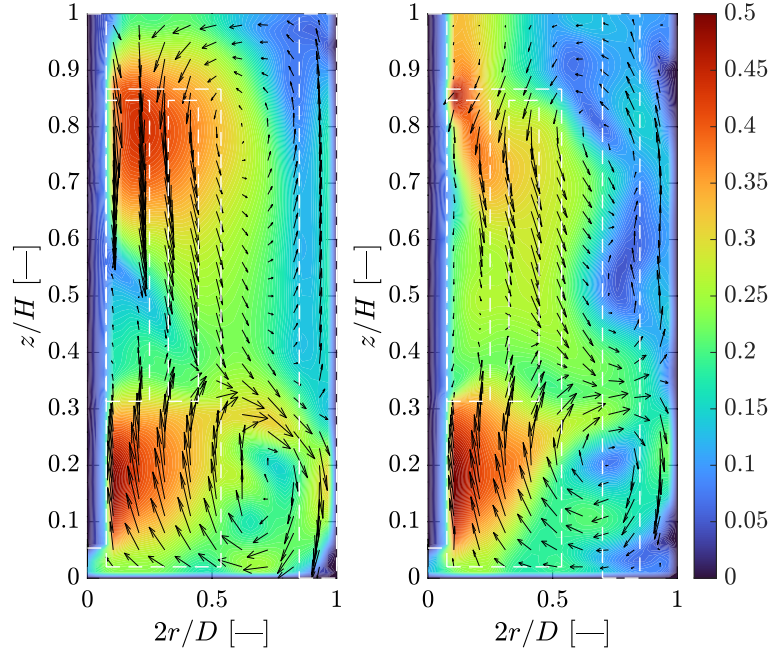$$f = \frac{\tau_{\mathrm{w}}}{\rho v_\theta^2/2} \tag{3.9}$$

Figure 3.7: Dimensionless velocity magnitude for the MAXBLEND® impeller; (left) $B_C = 0$, (right) $B_C = 0.075$; note that the velocity magnitude was normalized by U_0.

As reviewed above in Equation (3.2), Shiobara et al.[2] showed an analogy between momentum transfer and heat transfer using the friction factor defined by Equation (3.9) so that this chapter discussed this friction factor as well. The present work calculated τ_w based on the slip velocity u_w^* to obtain the friction factor as follows.

$$
\begin{aligned}
\tau_w &= \mu \left. \frac{\partial u_\theta}{\partial r} \right|_{\text{wall}} \\
&= \rho u_w^{*\,2}
\end{aligned}
\tag{3.10}
$$

Figures 3.8 and 3.9 present axial profiles of the time-averaged friction factor for vessels with and without baffle clearance using the MAXBLEND®

impeller. Three azimuthal positions are compared: the center between two baffles, in front of a baffle, and behind a baffle. The impeller rotated counterclockwise. The continuous solid line in each diagram represents the value calculated by the correlation equation of the friction factor for large impellers, including the MAXBLEND® impeller.[21] In the case without baffle clearance, the friction factor had a maximum value around the paddle-type zone of the impeller ($z/H < 0.4$) where tangential flow is strong. In contrast, a much smaller friction factor can be seen in the range of $z/H > 0.4$.

In the case without baffle clearance, the friction factor at $z/H < 0.4$ decreased. In addition, while the friction factor between baffles ($\theta = 45°$) slightly changed at $z/H > 0.4$, that around a baffle increased, especially behind the baffle as shown in Figure 3.10. Here, the friction factor ratio was defined as the ratio of two friction factors, $f|_{B_C=0.075}/f|_{B_C=0}$. Generally, an increase in velocity in the turbulent region far from the wall leads to a decrease in the boundary thickness, consequently, the friction factor increases. It is, therefore, concluded that this enhancement of the friction factor may have been caused by the increase in flow velocity around baffles.

According to the analogy in transport phenomena, the increase in the friction factor also significantly impacts mass transfer at the vessel wall. In a mineral processing plant, the hard deposit is supposed to form on the wall where the mass transfer is poor, especially behind baffles. Considering the results here, low values of the friction factor at the upper part of the sidewall around baffles correlate to the small transfer coefficient and result in a higher potential for material deposition. Furthermore, the improvement of mass transfer with baffle clearance, which corresponds to the increase in friction
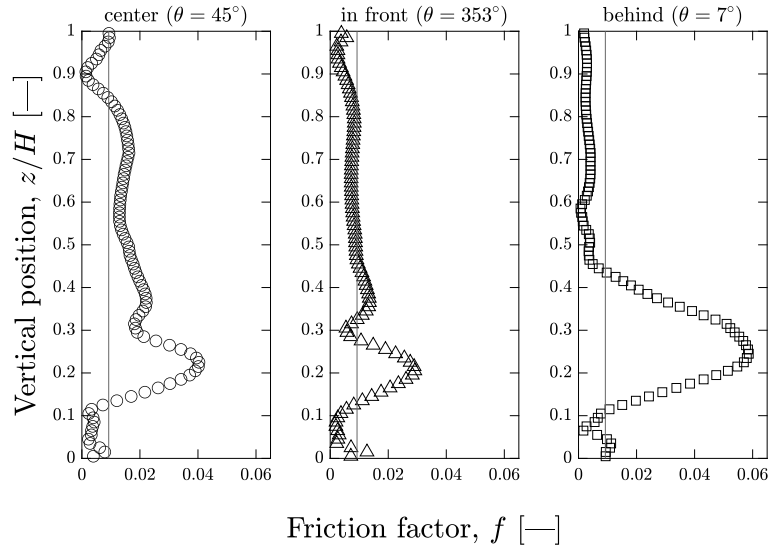
71

Figure 3.8: Axial profiles of the friction factor for the MAXBLEND®
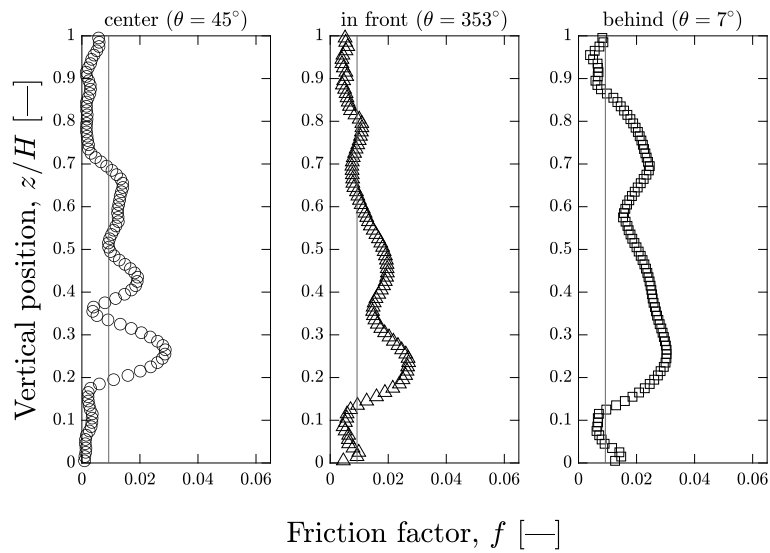impeller without baffle clearance, $B_\mathrm{C} = 0$.

Figure 3.9: Axial profiles of the friction factor for the MAXBLEND®
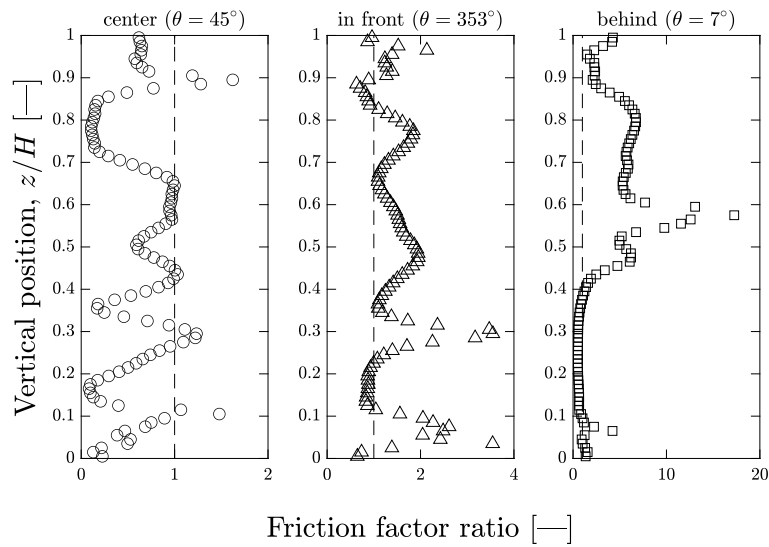impeller with baffle clearance, $B_\mathrm{C} = 0.075$.

Figure 3.10: Effect of adding baffle clearance on the friction factor.

factor, potentially reduces the scale adhesion in a baffled vessel. However, it should be noted that, although the friction factor may play a crucial role in the solid-liquid process, supersaturation or energy balance must be taken into account as well. The next chapter experimentally investigated and discussed the effect of adding baffle clearance on scaling.

Although baffles play a significant role in enhancing mixing performance in an agitated vessel, they may lead to undesirable results in some processes with heat control. The sidewall of an agitated vessel with jackets can be thermally damaged where the local heat transfer is poor. This poor heat transfer region may be predicted by detecting the region with a low friction factor, resulting in a low heat transfer coefficient. Considering this point, installing baffle clearance can be a reasonable option to avoid this problem.
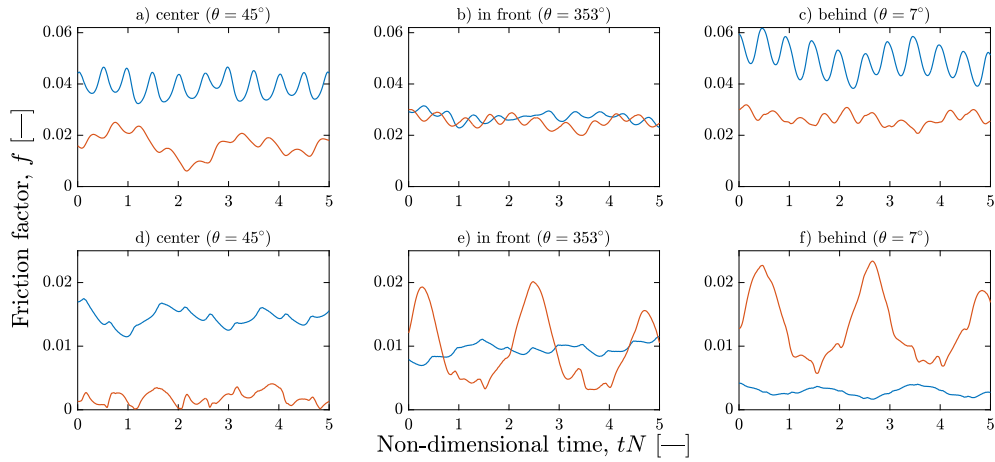
73

Figure 3.11: Variation of the friction factor over time: blue lines represent $B_C = 0$ and orange lines represent $B_C = 0.075$, respectively; (a-c) $z/H = 0.2$, (d-e) $z/H = 0.8$.

3.3.4 Temporal variation of the friction factor

Figure 3.11 indicates comparison of the time variation of the friction factor at $z/H = 0.2$ and 0.8. At $z/H = 0.2$, regardless of the existence of baffle clearance, the time variation of the friction factor had a characteristic frequency equal to 2 times the rotational frequency of the impeller. This resulted from the strong tangential flow induced by the fluid discharge from the paddle of the MAXBLEND® impeller. At $z/H = 0.8$, a remarkably large amplitude of the fluctuation of the friction factor was observed around a baffle. This large-scale fluctuation of the friction factor directly relates to the boundary layer thickness of momentum and heat transfer. Indeed, the heat transfer can be enhanced by an intermittent surface renewal of the boundary layer.[22] Therefore, further investigation on the effect of the width of the baffle clearance on the fluctuation of the friction factor is necessary to establish a global correlation of heat transfer with Reynolds number and baffle clearance.

74

3.4　Conclusions

The present chapter numerically investigated the effects of adding clearance between baffles and the sidewall on the friction factor in a turbulent agitated vessel equipped with a MAXBLEND® impeller. The velocity distribution near the wall using a paddle impeller was compared with the estimation by a model to validate the calculated results. The SST k-ω turbulent model provided a successful prediction not only in the fully turbulent region but in the viscous sublayer in the agitated vessel. Baffle clearance deformed the circulation flow in the vessel, and the flow became much complex. While the large value of friction factor at the sidewall was observed in the range with a strong discharge flow, the friction factor was smaller in the other vertical positions. The friction factor drastically increased by adding baffle clearance, especially around baffles, which should reduce the material deposition in the vessel. In addition, a large-scale fluctuation of friction factor was found, which may lead to the further enhancement of the heat/mass transfer.

Nomenclature

b = height of impeller [m]

c_p = specific heat $[\mathrm{J\,kg^{-1}\,K^{-1}}]$

B_C = clearance between tank wall and baffles [m]

B_H = length of baffle [m]

B_W = width of baffle [m]

d = diameter of impeller [m]

D = diameter of vessel [m]

f = friction factor [—]

h = heat transfer coefficient $[\mathrm{W\,m^{-2}\,K^{-1}}]$

H = height of liquid in the tank [m]

j_H = j-factor for heat transfer [—]

k = turbulent kinetic energy $[\mathrm{m^2\,s^{-2}}]$

m = correlation parameter in Equation (3.2) [—]

n_B = the number of baffles [—]

N = impeller rotational speed $[\mathrm{s^{-1}}]$

Pr = Prandtl number, $(= c_\mathrm{p}\mu/\lambda)$ [—]

r = radial coordinate [m]

r_d = radius of impeller [m]

Re_d = impeller Reynolds number, $(= Nd^2/\nu)$ [—]

u_w^* = friction velocity $[\mathrm{m\,s^{-1}}]$

u_z = axial velocity $[\mathrm{m\,s^{-1}}]$

u_θ = tangential velocity $[\mathrm{m\,s^{-1}}]$

u^+ = dimensionless velocity, $(= u_\theta/u_\mathrm{w}^*)$ [—]

u^{++} = dimensionless velocity, $(= u_\theta^+ (\beta D/md))$ [—]

U = velocity at the edge of the turbulent boundary layer $[\mathrm{m\,s^{-1}}]$

U_0 = impeller tip velocity $[\mathrm{m\,s^{-1}}]$

v_θ = characteristic velocity, $(= \beta U_0/2)$ $[\mathrm{m\,s^{-1}}]$

y = distance from the wall [m]

y^+ = dimensionless distance, $(= yu_\mathrm{w}^*/\nu)$ [—]

y^{++} = dimensionless distance, $(= y^+ (\beta D/md))$ [—]

z = axial coordinate [m]

Greek letters

β = coefficient, $(= 2\ln(D/d)/\{(D/d) - (d/D)\})$ [—]

ε = turbulent eddy dissipation rate $[\mathrm{m^2\,s^{-3}}]$

θ = azimuthal coordinate [°]

λ = thermal conductivity $[\mathrm{W\,m^{-1}\,K^{-1}}]$

μ = liquid viscosity $[\mathrm{Pa\cdot s}]$

μ_t = eddy viscosity $[\mathrm{Pa\cdot s}]$

ν = kinetic viscosity $[\mathrm{m^2\,s^{-1}}]$

ρ = liquid density $[\mathrm{kg\,m^{-3}}]$

τ_w = shear stress at the wall [Pa]

ω = specific turbulent dissipation rate $[\mathrm{s^{-1}}]$

References

(1) Hiraoka, S.; Kato, Y.; Iwata, S.; Tada, Y.; Sakai, H.; Yamaguchi, T.; Yamamura, M.; Nagasaka, I.; Shiobara, K. "Estimation of Tangential Velocity near Side Wall of Fully Turbulent Agitated Vessel without Baffles," *Journal of Chemical Engineering of Japan* **2006**, *39*, 583–586.

(2) Shiobara, K.; Hiraoka, S.; Kato, Y.; Iwata, S.; Yamaguchi, T.; Yamamura, M. "On the Similarity of Heat and Momentum Transfer at the Side Wall of a Fully Turbulent Agitated Vessel without Baffles," *Kagaku Kogaku Ronbunshu* **2007**, *33*, 288–293.

(3) Sedahmed, G.; El-Taweel, Y.; Abdel-Aziz, M.; El-Naqeara, H. "Mass and heat transfer enhancement at the wall of cylindrical agitated vessel by turbulence promoters," *Chemical Engineering and Processing: Process Intensification* **2014**, *80*, 43–50.

(4) Grisafi, F.; Brucato, A.; Rizzuti, L. "Solid liquid mass transfer coefficients in mixing tanks: Influence of side wall roughness," *IChemE Symp. Ser.* **1994**, *136*, 571–578.

(5) Kato, Y.; Kamei, N.; Tada, Y.; Iwasaki, Y.; Nagatsu, Y.; Iwata, S.; Lee, Y.-S.; Koh, S.-T. "Transport Phenomena around Cylindrical Baffles in an Agitated Vessel Measured by an Electrochemical Method," *Journal of Chemical Engineering of Japan* **2007**, *40*, 611–616.

(6) Calderbank, P.; Moo-Young, M. "The continuous phase heat and mass-transfer properties of dispersions," *Chemical Engineering Science* **1961**, *16*, 39–54.

(7) Mizushina, T.; Ito, R.; Hiraoka, S.; Ibusuki, A.; Sakaguchi, I. "TRANSPORT PHENOMENA AT THE WALL OF AGITATED VESSELS," *Journal of Chemical Engineering of Japan* **1969**, *2*, 89–94.

(8) Cudak, M.; Karcz, J.; Kielbus-Rapala, A. "Transport phenomena in an agitated vessel with an eccentrically located impeller," *Chemical Papers* **2011**, *65*, 147–155.

(9) Cudak, M.; Karcz, J. "The effects of eccentricity of axial flow impeller on the momentum transfer process in an agitated vessel," *Experimental Thermal and Fluid Science* **2013**, *44*, 385–391.

(10) Wu, J.; Parthasarathy, R.; Nguyen, B. "Scale growth in agitated neutralization tanks," *Minerals Engineering* **2021**, *160*, 106697.

(11) Menter, F. In, 1993, pp 93–2906.

(12) Wilcox, D. C. "Reassessment of the scale-determining equation for advanced turbulence models," *AIAA Journal* **1988**, *26*, 1299–1310.

(13) Yoshida, T.; Nagase, Y.; Kakumoto, M.; Hasegawa, T.; Matoba, T. "Experimental Investigation of the Similarity of Flow Pattern in an Unbaffled Agitated Vessel," *Kagaku Kogaku* **1973**, *37*, 1038–1044, a1.

(14) Dong, L.; Johansen, S.; Engh, T. "Flow induced by an impeller in an unbaffled tank—I. Experimental," *Chemical Engineering Science* **1994**, *49*, 549–560.

(15) Nagata, S.; Yamamoto, K.; Ujihara, M. "Flow Patterns of Liquid in a Cylindrical Mixing Vessel without Baffles," *Kagaku Kogaku* **1959**, *23*, 130–137.

(16) Hiraoka, S.; Shiobara, K.; Kato, Y.; Iwata, S.; Tada, Y.; Yamaguchi, T.; Yamamura, M. "Universal Expression of Tangential Velocity Distribution near Side Wall of a Fully Turbulent Agitated Vessel without Baffles," *Journal of Chemical Engineering of Japan* **2007**, *40*, 666–672.

(17) Tamburini, A.; Brucato, A.; Ciofalo, M.; Gagliano, G.; Micale, G.; Scargiali, F. "CFD simulations of early- to fully-turbulent conditions in unbaffled and baffled vessels stirred by a Rushton turbine," *Chemical Engineering Research and Design* **2021**, *171*, 36–47.

(18) Hidalgo-Millán, A.; Zenit, R.; Palacios, C.; Yatomi, R.; Horiguchi, H.; Tanguy, P. A.; Ascanio, G. "On the hydrodynamics characterization of the straight Maxblend impeller with Newtonian fluids," *Chemical Engineering Research and Design* **2012**, *90*, 1117–1128.

(19) Mancilla, E.; Yatomi, R.; Zenit, R.; Ascanio, G. "Hydrodynamic Characterization of Three Axial Impellers under Gassed and Ungassed Conditions," *Journal of Chemical Engineering of Japan* **2016**, *49*, 894–903.

(20) Hiraoka, S.; Yamada, I.; Doi, N.; Takeda, H.; Kawai, A.; Usui, Y.; Ito, R. "General Correlation Method of Power Consumption in Agitated Vessels—Correction of characteristic velocity—," *Bull. Nagoya Inst. Tech.* **1975**, *26*, 239–245.

(21) Kato, Y.; Obata, A.; Kato, T.; Furukawa, H.; Tada, Y. "Power Consumption of Two-Blade Wide Paddle Impellers," *Kagaku Kogaku Ronbunshu* **2012**, *38*, 139–143.

(22) Kataoka, K.; Suguro, M.; Degawa, H.; Maruo, K.; Mihata, I. "The effect of surface renewal due to largescale eddies on jet impingement heat transfer," *International Journal of Heat and Mass Transfer* **1987**, *30*, 559–567.

Chapter 4

Effect of baffle clearance on material deposition on the vessel wall

4.1 Introduction

Scale, as briefly summarized in chapter 1, has been a significant issue in many industries with solid-liquid processes. The precedent experimental investigations showed successful suppression of the material deposition on the wall by controlling hydrodynamics in the agitated vessel. Nawrath et al.[1] experimentally examined scale growth in alumina refineries and suggested that a slurry flow velocity of more than 2.9 m/s near the walls of the vessel could reduce the rate of scale growth to zero on the vessel walls. Wu et al.[2] applied swirl flow agitator to a mineral process and showed that the growth of scale could be reduced compared to a conventional draft tube agitator sys-

tem. Davoody et al.[3] conducted a qualitative and quantitative investigation on the scale deposition on the wall of an agitated vessel and showed that the scale thickness was lower in the non-baffled vessel than in the baffled vessel.

Chapter 3 reported the drastic increase in the friction factor around baffles by adding baffle clearance. This result implies that the baffle clearance contributes to the reduction of scale on the vessel wall. The present chapter, as a verification of the consequence in chapter 3, experimentally investigated the effect of clearance between baffles and the vessel wall on the scale deposition to overcome scale formation behind baffles. The experimental method presented by Davoody et al.[4] was used as a model of scale deposition, which utilized the production reaction of magnesium hydroxide [$Mg(OH)_2$]. The amount of scale and its distribution on the sidewall were discussed with the flow velocity in the tank obtained by numerical simulation.

4.2 Experimental

4.2.1 Quantification of scale formation

The disassemblable vessel made of stainless steel was used for scale quantification experiments. Agitation was provided by a MAXBLEND® impeller which was set to the vertical axis of the tank and driven by a motor as shown in Figure 4.1. Two baffle arrangement was tested, i.e., the case with and without clearance between baffles and vessel wall ($B_C/D = 0, 0.06$). Table 4.2.2 gives the geometric details of the tank, impeller, and baffles.

The scale used in this study is magnesium hydroxide [$Mg(OH)_2$] formed

83

from the chemical reaction between calcium hydroxide [$Ca(OH)_2$] and magnesium chloride [$MgCl_2$]. The precipitate of $Mg(OH)_2$ forms when pH is over 12 due to the reaction of dissociation of the weak acid. A 500 mL of $Ca(OH)_2$ solution with the concentration of 0.6 M and a 500 mL of 0.5 M sodium carbonate [Na_2CO_3] solution were prepared as the initial liquid and fed into the vessel. The vessel filled with the initial liquid was placed into a thermostatic bath to keep the fluid temperature at 80 °C since the hot surface of the wall encourages the deposition of $Mg(OH)_2$. After the liquid temperature reaching to a steady-state, 15 g of $MgCl_2$ powder was gradually added into the tank with agitation. The duration of the experimental run was 45 min to precipitate magnesium hydroxide on the vessel wall sufficiently. After pumping out, the weight of the formed scale was measured as the difference in the weight of the vessel before and after the experiment. The more detailed experimental methodology can be referred to in the paper of Davoody et al.[4] The present thesis shows the results when the rotational speed of the impeller was in the range of $N = 200$–280 rpm since the scale could not be quantified at the higher rotational speeds.

4.2.2 Flow velocity and power consumption measurement

Flow velocity in the agitated vessel was measured by an ultrasonic velocity profiler (UVP) to validate the numerical results. UVP is a powerful tool to obtain flow field along the ultrasonic beam axis directly and is now used not only in the pipe or duct flow[5,6] but in the flow in complex geometries.[7] An
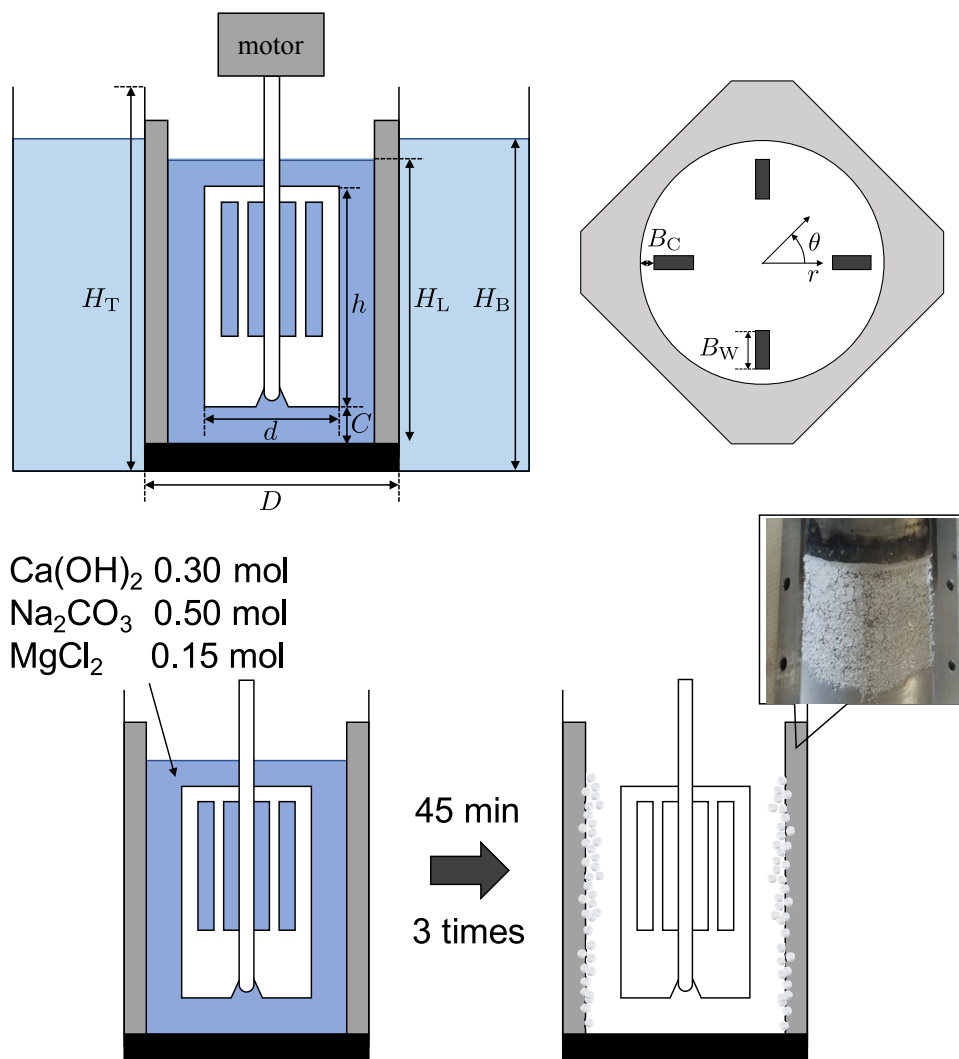
Figure 4.1: Schematic of experimental setup and procedure.

Table 4.1: Tank, impeller and baffle dimensions.

symbol	parameter	value
D	Tank diameter	100 mm
H_T	Tank height	200 mm
H_L	Liquid height	160 mm
H_B	Water bath height	220 mm
d	Impeller diameter	62.8 mm
h	Impeller height	139 mm
C	Impeller clearance from tank bottom	10 mm
$B_\mathrm{L}/H_\mathrm{L}$	Dimensionless baffle height	1
B_W/D	Dimensionless baffle width	0.1
B_C/D	Dimensionless baffle clearance	0 or 0.06
—	The number of baffles	4

ultrasonic pulse wave is irradiated to the fluid containing tracer particles as shown in Figure 4.2, and the probe then detects the Doppler shift frequency of echoed ultrasound as a function of time. Flow velocity is calculated based on the proportional relationship with the Doppler shift frequency. Detailed principle of UVP measurement can be seen in the literature by Takeda.[8]

A commercial UVP device (UVP-DUO, Met-Flow SA) and co-polyamide particles were used. The particle size was 80–200 µm in diameter, and the density was 1070 kg m^{-3}. The ultrasonic pulse was emitted from the transducer at a pulse repetition frequency of 1.87 kHz. The diameter of the sensor was 8 mm, and the basic frequency was 4 MHz. The geometrical configurations of the impeller and acrylic-made vessel for UVP measurement were the same as those shown in Figure 4.1 and Table .

The power consumption of the impeller was measured with a torque meter (i-stirrer ls600, Trinity-Lab Inc.). The power consumption P was calculated by Equation (4.1) using the rotational speed of the impeller and average
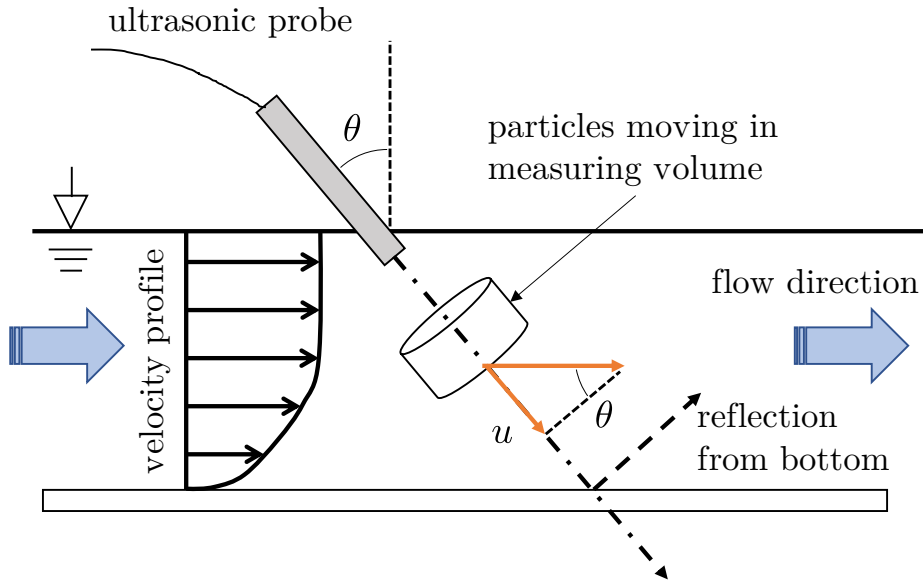
Figure 4.2: Schematic picture of UVP measurement, reproduction from UVP-DUO Monitor User's Guide[9] by the author.

torque T measured for at least $180\,\text{s}$ in each run.

$$P = 2\pi NT \qquad (4.1)$$

The tank, impeller, and baffle were the same as those used in UVP measurement. All measurements were done using the tap water at room temperature.

4.3 Numerical setup

In the present chapter as well, the flow velocity and flow pattern were numerically obtained by a CFD software RFLOW (Rflow Co., Ltd.). The fluid was considered as an incompressible Newtonian fluid having the same prop-

erties as water. The conservation and Navier-Stokes equations were solved. The SIMPLE algorithm was applied to couple pressure and velocity. Although chapter 3 used the SST k-ω model, the standard k-ε model[10] was applied in the present chapter for reasons of stability and computational cost. The boundary conditions and the established computational domains are the same as those in chapter 3. The mesh number was $40 \times 120 \times 80$ in the radial, azimuthal and axial directions, respectively. The total number of numerical cells was more than 3.8×10^5.

4.4 Results and Discussion

4.4.1 Velocity validation of numerical results

This chapter will discuss the tangential velocity later. However, the measurement of tangential velocity was difficult due to the configuration of the experimental apparatus. Alternatively, the numerical results were validated by experimental results in terms of the axial velocity distribution.

The time-averaged axial velocity during $100\,\mathrm{s}$ was obtained from the time series velocity data from the UVP measurement. Numerical results of the velocity were also averaged in time. Figure 4.3 shows the vertical profiles of the axial velocity component along the line defined by $2r/D = 0.9$ and $\theta = 45°$ in the cylindrical coordinate system. As depicted in Figure 4.3, the good agreement of the velocity distribution can be seen between experimental and numerical results. Only some small discrepancies existed in the simulation and experiment. However, two local maxima were observed, and the values
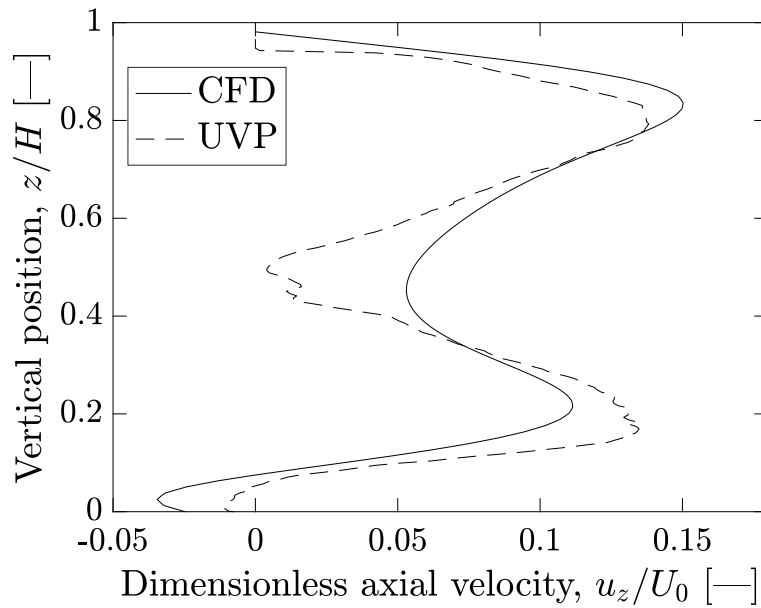
88

Figure 4.3: Comparison of dimensionless axial velocity profile in the vertical direction between numerical and experimental results.

at the two maxima were very similar. It indicated that the simulation model was reliable, and the validity of the numerical procedure was confirmed.

4.4.2 Effect of impeller rotational speed on scaling

Figure 4.4 describes the effects of the rotational speed of the impeller and baffle clearance on scale weight. The scale weight decreased almost linearly with the impeller rotational speed regardless of the configuration of baffle clearance. This tendency is consistent with the case of a small agitator, the Lightnin A310,[4] and also can be seen in the case of pipe flow.[1] As Wu et al.[2] pointed out, removal of material deposit can co-occur with the scale formation. Therefore, in this complex process, this result shows that the removal of material deposits was much more accelerated than that of scale
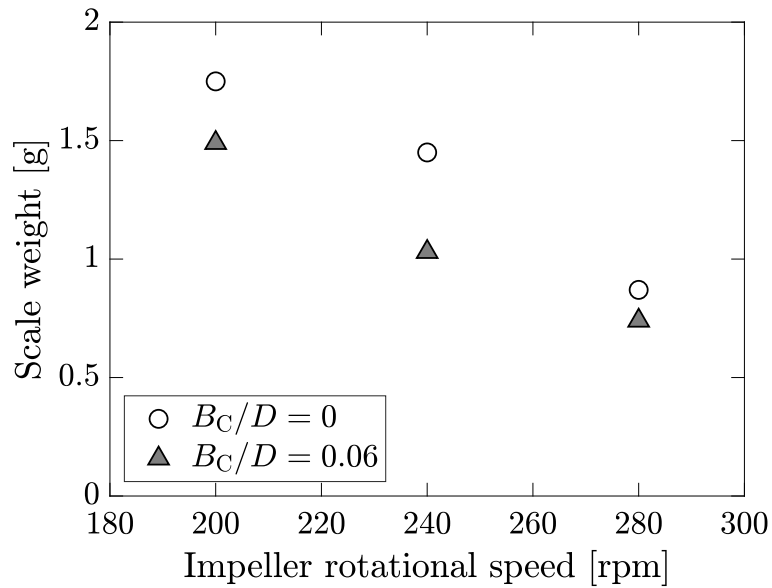
89

Figure 4.4: Effects of the impeller rotational speed and baffle clearance on the weight of formed scale.

growth.

4.4.3 Effect of baffle clearance on scale deposition

Figures 4.5 and 4.6 illustrate the distribution of formed scale on the tank wall with and without baffle clearance ($B_C/D = 0, 0.06$), respectively. In the photographs for the case without baffle clearance as shown in Figure 4.5, baffles were attached to both sides of the disassembled vessel walls, which were illustrated as striped boxes. On the other hand, the baffle was placed on the center for the case with baffle clearance as shown in Figure 4.6. In all the photographs, fluid flowed from left to right. In the case without baffle clearance, the smaller weight of the scale was deposited on the vessel wall in front of the baffles, while the weight of the scale was larger behind the

baffles. A decrease in scale thickness and area of the sidewall covered by scale was observed for $B_C/D = 0.06$, which resulted in the decrease in the weight of scale by the installation of baffle clearance as described in Figure 4.4. Moreover, the suppression of deposition behind baffles was significantly improved in the case with baffle clearance. These results agree with the expectation obtained in chapter 3 that the increase in the friction factor contributes to the suppression of scale.

Figure 4.7 shows the numerically obtained tangential velocity between a baffle and sidewall when the impeller position is $\theta = 45°$. The baffle is placed at $\theta = 0°$ and flow goes through right to left (counterclockwise) in Figure 4.7. When $B_C/D = 0$, the flow impinged on baffles, which resulted in a decrease in tangential velocity in front of a baffle and behind a baffle. This flow impingement caused erosion of scale in front of baffles, and a decrease in tangential velocity behind baffles promoted scale growth, which was observed in Figure 4.5. In the case with baffle clearance ($B_C/D = 0.06$), the velocity decrease around baffles completely disappeared, and a significant increase in flow velocity near the sidewall can be seen. Because of contraction flow, tangential velocity drastically increased through the gap between baffles and sidewall. Consequently, this higher flow velocity eroded deposits, which resulted in a decrease in scale weight, as can be seen in Figure 4.4.

4.4.4 Effect of baffle clearance on power consumption

Most processes using agitated tanks are designed based on the power diagram of the impeller since main equipment such as a motor must have a
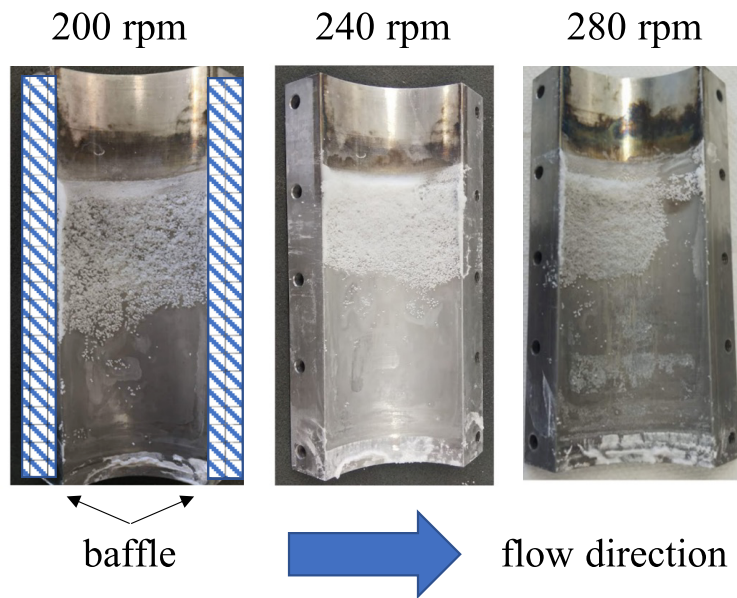
200 rpm   240 rpm   280 rpm

baffle   flow direction

Figure 4.5: Distribution of scale deposition for $B_\mathrm{C}/D = 0$.
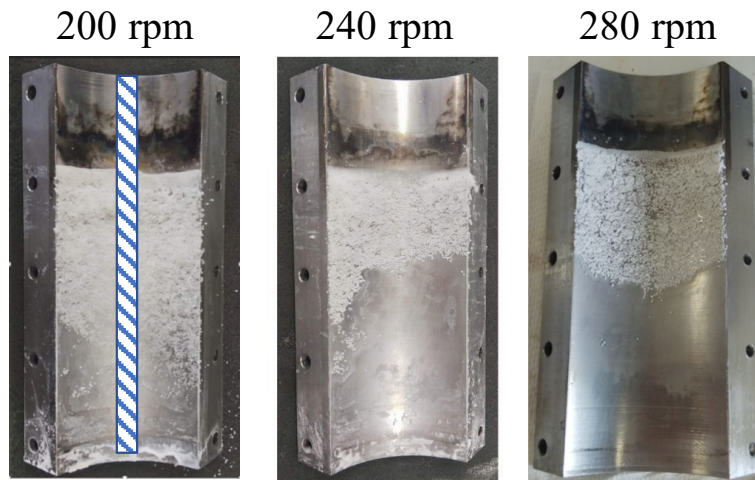
200 rpm   240 rpm   280 rpm

Figure 4.6: Distribution of scale deposition for $B_\mathrm{C}/D = 0.06$.
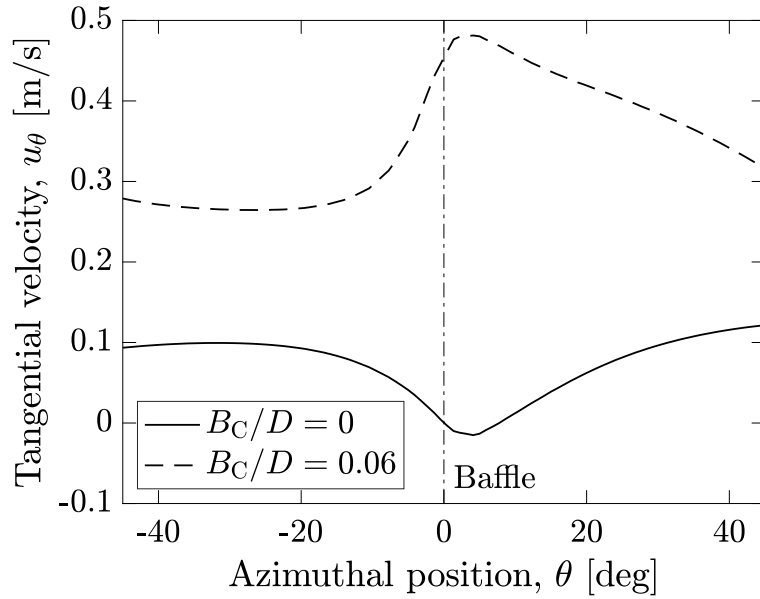
Figure 4.7: Tangential velocity profile in azimuthal direction at $2r/D = 0.92$, $z/H = 0.5$ at $N = 240\,\mathrm{rpm}$.

sufficient impact on power consumption. The power consumption directly affects the economy of the process. Figure 4.8 shows the relationship between the rotational speed of the impeller and the power consumption by the correlation between the Reynolds number Re_d $(= \rho N d^2/\mu)$ and the power number N_p $(= P/\rho N^3 d^5)$. The tested impeller rotational speed in scale experiment $N = 200$–$280\,\mathrm{rpm}$ corresponds to Re_d in the range of 1.3–1.8×10^4. It was found that, in the turbulent region, installation of baffle clearance slightly saved power consumption. However, it did not have a significant impact on energy reduction. Considering the decrease in the scale deposition shown in Figure 4.4, installation of baffle clearance can reduce scale under the same energy consumption without adding chemical antiscalants and can be a promising approach to intensify the process efficiency from the viewpoint
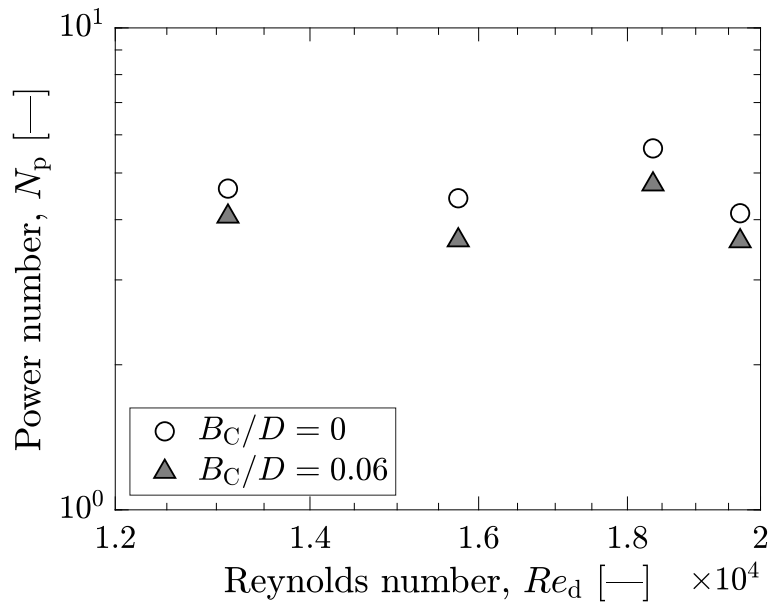
93

Figure 4.8: Relationship between the power number and the Reynolds number.

of operational costs and process safety.

4.5 Conclusions

The present chapter experimentally investigated the effects of clearance between baffles and vessel wall on the material deposition in turbulent flow regime, using the MAXBLEND® impeller. The increase in the rotational speed of the impeller suppressed scale growth both in cases with and without baffle clearance. In the case without baffle clearance, the smaller scale weight was obtained due to the flow impingement on baffles, which enhanced the removal of the scale deposition. In contrast, the lower velocity magnitude behind the baffles resulted in the formation of more scale in amount. Installation of baffle clearance caused contraction flow between the tank wall

and baffles, and, consequently, higher flow velocity reduced the scale deposition there. Measurement of torque of the rotating impeller showed that the installation of baffle clearance did not reduce energy consumption. However, from the viewpoint of operating cost and process safety, it can be a promising approach to improve process efficiency.

Nomenclature

B_C = clearance between tank wall and baffles [m]

B_L = length of baffle [m]

B_W = width of baffle [m]

C = clearance between tank bottom and impeller [m]

d = diameter of impeller [m]

D = diameter of tank [m]

h = height of impeller [m]

H_B = height of water bath [m]

H_L = height of liquid [m]

H_T = height of tank [m]

N = impeller rotational speed [s^{-1}]

N_p = power number, ($= P/\rho N^3 d^5$) [—]

P = power consumption [W]

r = radial coordinate [m]

Re_d = impeller Reynolds number, ($= \rho N d^2/\mu$) [—]

T = time-averaged torque [N m]

u = velocity [m s^{-1}]

u_z = vertical velocity [m s^{-1}]

u_θ = tangential velocity [m s^{-1}]

U_0 = impeller tip velocity [m s^{-1}]

z = axial coordinate [m]

Greek letters

θ = azimuthal coordinate [°]

μ = liquid viscosity $[\mathrm{Pa} \cdot \mathrm{s}]$

ρ = liquid density $[\mathrm{kg\,m^{-3}}]$

References

(1) Nawrath, S.; Khan, M.; Welsh, M. "An experimental study of scale growth rate and flow velocity of a super-saturated caustic-aluminate solution," *International Journal of Mineral Processing* **2006**, *80*, 116–125.

(2) Wu, J.; Lane, G.; Livk, I.; Nguyen, B.; Graham, L.; Steginik, D.; Davis, T. "Swirl flow agitation for scale suppression," *International Journal of Mineral Processing* **2012**, *112-113*, Special Issue Communion 2009, 19–29.

(3) Davoody, M.; Graham, L. J.; Wu, J.; Witt, P. J.; Madapusi, S.; Parthasarathy, R. "Mitigation of scale formation in unbaffled stirred tanks-experimental assessment and quantification," *Chemical Engineering Research and Design* **2019**, *146*, 11–21.

(4) Davoody, M.; Graham, L. J.; Wu, J.; Youn, I.; Abdul Raman, A. A.; Parthasarathy, R. "A Novel Approach To Quantify Scale Thickness and Distribution in Stirred Vessels," *Industrial & Engineering Chemistry* **2017**, *56*, 14582–14591.

(5) Tezuka, K.; Mori, M.; Suzuki, T.; Kanamine, T. "Ultrasonic pulse-Doppler flow meter application for hydraulic power plants," *Flow Measurement and Instrumentation* **2008**, *19*, ISUD 5: The 5th International Symposium on Ultrasonic Doppler Methods for Fluid Mechanics and Fluid Engineering, 155–162.

(6) Murakawa, H.; Muramatsu, E.; Sugimoto, K.; Takenaka, N.; Furuichi, N. "A dealiasing method for use with ultrasonic pulsed Doppler in measuring velocity profiles and flow rates in pipes," *Measurement Science and Technology* **2015**, *26*, 085301.

(7) Kotzé, R.; Wiklund, J.; Haldenwang, R.; Fester, V. "Measurement and analysis of flow behaviour in complex geometries using the Ultrasonic Velocity Profiling (UVP) technique," *Flow Measurement and Instrumentation* **2011**, *22*, 110–119.

(8) Takeda, Y., "Ultrasonic Doppler Velocity Profiler for Fluid Flow," Springer Japan: 2012.

(9) "UVP-DUO Monitor User's Guide," Met-Flow SA: Lausanne, 2014.

(10) Launder, B.; Spalding, D. "The numerical computation of turbulent flows," *Computer Methods in Applied Mechanics and Engineering* **1974**, *3*, 269–289.

Chapter 5

Conclusions

This dissertation aimed to obtain beneficial guidelines to design processes in the agitated vessel. The conclusions of each chapter are as follows.

Chapter 2 investigated a particulate process in the vessel agitated by the Rushton turbine. The distribution of shear rate in the vessel leads to difficulty predicting the agglomeration behavior of solid particles. A representative shear rate for particle agglomeration was defined based on local residence time to take shear history into account. Chapter 2 offers the following results and remarks.

- Bimodal particle size distributions were experimentally obtained so that the population balance model was simplified. The proposed representative shear rate successfully predicted experimental data using the simplified model than Metzner-Otto's shear rate and volume-averaged shear rate.

- The shear rate obtained by fitting experimental data using the simpli-

fied model showed good agreement with the proposed representative shear rate in various particle concentrations.

Chapter 3 numerically analyzed the effect of baffle clearance based on the transport phenomena in the turbulent regime. The used turbulent model, SST k-ω model, was validated with the theoretical data in a non-baffled vessel using a paddle impeller. The friction factors at the sidewall were compared among the cases with and without baffle clearance. Besides, this chapter discussed the advantage of installing baffle clearance in practical processes based on the analogy. Chapter 3 clarified the following contents.

- The SST k-ω model provided an excellent prediction not only in the fully turbulent flow region but in the viscous sublayer in the agitated vessel.

- A strong discharge and tangential flow resulted in the large value of friction factor at the sidewall of the vessel. The small friction factor was smaller at the other vertical position. The friction factor directly increased around the baffles by adding baffle clearance.

- A large scale of the fluctuation of friction factor was found, which may lead to the further enhancement of the physical transfer.

Chapter 4 experimentally investigated a practical process in the baffled vessel with the issue of material deposition on the vessel wall. Baffle clearance was installed to overcome the scale formation around baffles. The following results were obtained in Chapter 4.

101

- The increase in rotational speed of the impeller suppressed scale growth both in cases with and without baffle clearance.

- Installation of baffle clearance caused contraction flow between the tank wall and baffles, and, consequently, higher flow velocity reduced the scale deposition there as chapter 3 indicated.

- Measurement of torque of the rotating impeller showed that the installation of baffle clearance did not reduce energy consumption. Therefore, the installation of baffle clearance is a promising approach to improve process efficiency in the operating cost.

In chapter 2, this work proposed a new representative shear rate as a guideline to design the particle agglomeration processes in the agitated vessel and showed its applicability for the Rushton turbine. However, the investigation was limited to the particle concentration, where the suspension viscosity can be regarded as that of dispersed fluid. Practical particulate processes are often operated at higher particle concentrations to enhance productivity. Further investigations are needed whether the proposed representative shear rate provides successful prediction or not at higher particle concentrations to obtain a global guiding principle to design agglomeration processes. Additionally, the proposed representative shear rate should be applied to different impellers to clarify whether it works efficiently or not.

Among geometric configurations of the agitated vessel, this dissertation focused on the clearance between baffles and the sidewall of the vessel. Chapter 3 discussed the advantage of installing baffle clearance based on the analogy in physical transfers. As shown in Chapter 3, the friction factor has spa-

tial distribution in tangential and vertical directions, which indicates that a Nusselt-type correlation equation with distribution function is necessary to design baffled agitated vessels.

Chapter 4 clarified that the baffle clearance efficiently performed reducing scale on the sidewall. Furthermore, the other baffle configurations, including length, width, and shape, must affect the hydrodynamic flow in the vessel, which should be actively studied in the future.

Appendix A

Results of the agglomeration experiment using the MAXBLEND® impeller

Chapter 2 proposed a new representative shear rate and showed results of the agglomeration experiment using the Rushton turbine. The present appendix shares the experimental results of the MAXBLEND® impeller for reference. The preparation procedure of the used slurry can be found in chapter 2. The geometrical details of the MAXBLEND® impeller and the vessel are the same as those used in the UVP measurement in chapter 4, but the vessel has no baffles here.

The experimentally estimated representative shear rate shown in Figure A.2 was calculated by the same process in chapter 2. Figure A.2 includes the representative shear rate by Metzner and Otto. The constant k_s (larger one) was estimated by Furukawa et al.[1]
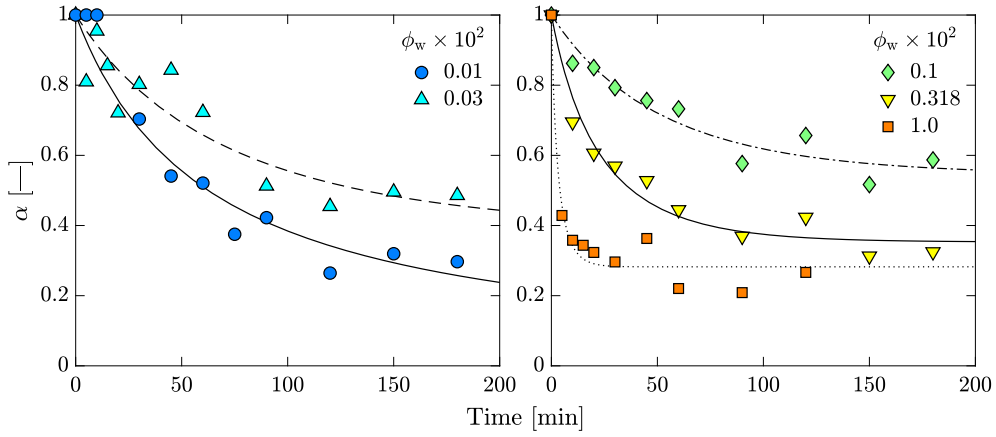
Figure A.1: Agglomeration process for different particle concentrations for the MAXBLEND® impeller at $N = 100\,\mathrm{rpm}$.
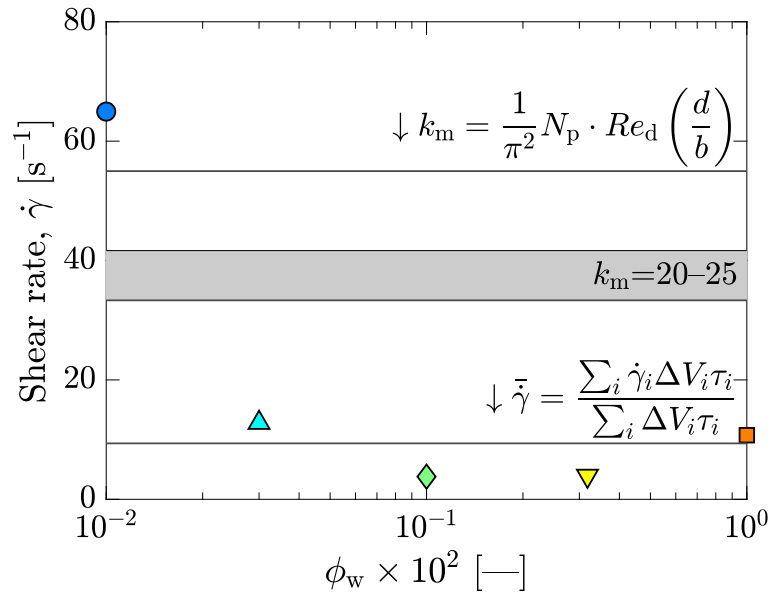
Figure A.2: Comparison between experimentally obtained shear rate and representative shear rates for the MAXBLEND® impeller in different particle concentrations at $N = 100\,\mathrm{rpm}$.
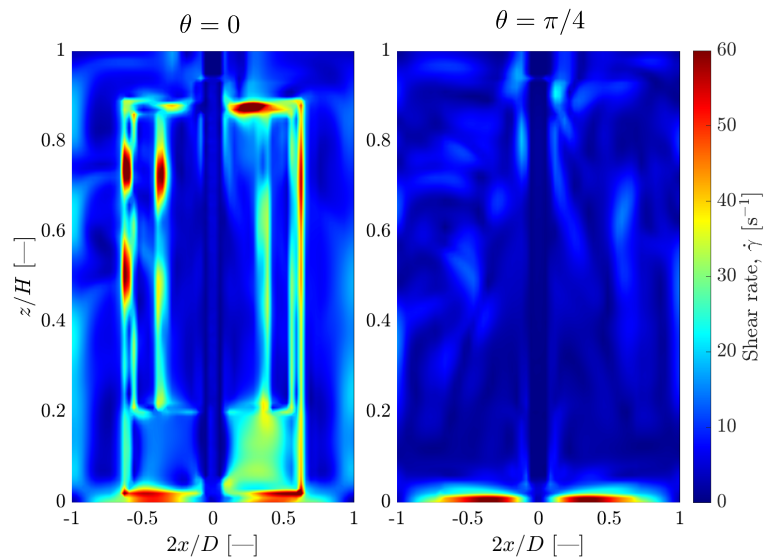
Figure A.3: Shear field in the vessel agitated by the MAXBLEND® impeller at $N = 100\,\mathrm{rpm}$.

References

(1) Furukawa, H.; Nakamura, N.; Kato, Y.; Nagumo, R.; Tada, Y. "Metzner-Otto Constant of Paddle Impeller with Two Large Blades in Shear-Thinning Fluid," *Kagaku Kogaku Ronbunshu* **2016**, *42*, 92–95.

Publications

Chapter 2 <u>Yusuke Ochi</u>; Ziqi Cai; Takafumi Horie; Yoshiyuki Komoda; Kuo-Lun Tung; Naoto Ohmura "Representative shear rate for particle agglomeration in a mixing tank," *Chemical Engineering Research and Design* **2021**, *171*, 73–79.

https://doi.org/10.1016/j.cherd.2021.04.017

Chapter 3 <u>Yusuke Ochi</u>; Katsuhide Takenaka; Yoshiyuki Komoda; Naoto Ohmura "Friction factor distribution at the side wall of a turbulent agitated vessel with baffles using MAXBLEND® impeller," *Industrial & Engineering Chemistry Research* **2022**, Published online.

https://doi.org/10.1021/acs.iecr.1c04229

Chapter 4 Eri Sato; <u>Yusuke Ochi</u>; Hiroo Horiguchi; Katsuhide Takenaka; Jie Wu; Rajarathinam Parthasarathy; Yoshiyuki Komoda; Naoto Ohmura "Effect of Baffle Clearance on Scale Deposition in an Agitated Vessel," *ACS Omega* **2021**, *6* (37), 24070–24074.

https://doi.org/10.1021/acsomega.1c03503

Acknowledgements

Before starting the Ph.D program, it seemed like a long tunnel of darkness. Indeed the life of a Ph.D student has never been easy, but I have certainly enjoyed this unique experience. During my studying period, I derived inspiration and received great help from multiple sources, so now I wish to express my deep gratitude to all those sources.

I am much indebted to my supervisor, Professor Naoto Ohmura, for sharing his knowledge, advising me with great insight, and letting me study following my own interests for six years. I could never accomplish my doctoral dissertation without his detailed guidance. I wish to express my sincere gratitude and deeply respectful feelings to him.

I am grateful to Associate Professor Yoshiyuki Komoda for examination of this work, the fruitful discussion, and the valuable advice with his energetic personality.

I would like to thank the committee members of the examination, Professor Hiroshi Suzuki and Professor Hitoshi Asano, for accepting the review of this work and giving beneficial advice.

My gratitude goes to Professor Kuo-Lung Tung of National Taiwan University for warmly welcoming me twice. I could have wonderful days in

108

Doctoral Dissertation, Kobe University

"Process design of solid-liquid mixing in agitated vessels based on transport phenomena", 109 pages

Submitted on January, 21, 2022

The date of publication is printed in cover of repository version published in Kobe University Repository Kernel.